Optimization and Tradeoff of DC Bus Voltage Ripple and DAB Current Stress in Two-Stage Single-Phase Converter by Double-Line-Frequency Power Control

Fei Xiong, *Member, IEEE*, Peng Wu, Hongyu Yang, Kaibi Zhang, and Dong Yan

***Abstract*—With consideration of double-line-frequency instantaneous power in two-stage single-phase system, a double-line-frequency power control method is proposed in this article to achieve optimization and tradeoff control between the current stress of dual-active-bridge (DAB) dc/dc converter and the dc bus voltage ripples in both sides. Different double-line-frequency powers in DAB will lead to different values of DAB current stress and dc bus voltage ripples in both sides. To find out the best double-line-frequency power in DAB, the optimal control trajectory (OCT) is proposed in this article so that the current stress of DAB can be minimized under any certain voltage ripple. An approximate analytical calculation method is derived to solve the optimal double-line-frequency power in OCT. The comparative analysis indicates that the approximate OCT has similar optimization effects as OCT. Based on the OCT, two tradeoff control methods for the DAB current stress and the dc bus voltage ripples are presented so that the current stress and the voltage ripples can be flexibly adjusted to adapt various load conditions. The initial phase of the single-phase ac load is also optimized to maximize the adjustable range of voltage ripple. The experimental results verify the feasibility and effectiveness of the proposed OCT and control methods.**

***Index Terms*—Current stress, double-line-frequency, dual-active-bridge (DAB), tradeoff, voltage ripple.**

I. Introduction

THE two-stage ac/dc+dc/dc is one of the most widely studied ac/dc converter systems. The system in Fig. 1 is one of the typical two-stage topologies [1]. It consists of an isolated bidirectional dc/dc converter, e.g., dual-active-bridge (DAB) converter and an ac/dc converter, e.g., single-phase H-bridge or three-phase full bridge. The two-stage ac/dc system has a wide application prospect [2] in electric vehicle charger, battery energy storage, and so on. Recently, the high-frequency isolated bidirectional dc/dc converter has also been applied to ac/dc hybrid microgrid [3], [4], [5]. As a result, the dc/dc converter has to face with hybrid load conditions (ac+dc).

Manuscript received 18 February 2023; revised 30 June 2023; accepted 2 August 2023. Date of publication 21 August 2023; date of current version 22 September 2023. This work was supported by the Science and Technology Research Program of Chongqing Municipal Education Commission under Grant KJQN202000620. Recommended for publication by Associate Editor A. Safaee. *(Corresponding author: Fei Xiong.)*

The authors are with the College of Automation, Chongqing University of Posts and Telecommunications, Chongqing 400065, China (e-mail: xiongfei@cqupt.edu.cn; s200331048@stu.cqupt.edu.cn; 1542472420@qq.com; zhangkb@cqupt.edu.cn; yandong@cqupt.edu.cn).

Color versions of one or more figures in this article are available at https://doi.org/10.1109/TPEL.2023.3306869.

Digital Object Identifier 10.1109/TPEL.2023.3306869

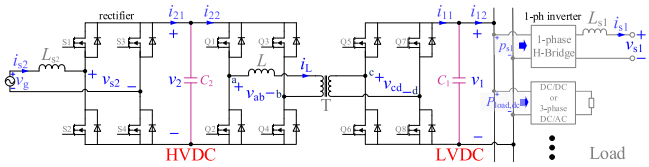

Fig. 1. Main circuit of the two-stage single-phase converter system.

In the two-stage single-phase converter system (see Fig. 1), the instantaneous power will fluctuate at twice the grid frequency (double-line-frequency) not only in the HVdc side but also in the LVdc side due to the inherent property of instantaneous power in single-phase ac grid or ac load. As a result, the double-line-frequency voltage ripple will arise in the dc buses directly. Conventionally, when the system serves as a power supply, the dc bus voltage in the LVdc side is regulated by dc/dc converter, while the dc bus voltage in HVdc side is regulated by H-bridge rectifier [6], [7]. The double-line-frequency power will be inevitably propagated into the dc/dc converter due to the conventional closed-loop control system [29], leading to remarkably increase of dc/dc current stress.

In the two-stage single-phase system, the suppression of the low-frequency fluctuations in the dc bus voltage and the dc–dc converter current stress are the two contradictory optimal control objectives for the double-line-frequency instantaneous power in dc/dc converter [8]. In the conventional dual-loop control method [7], only the closed-loop control bandwidth can be designed to regulate the dc bus voltage ripple and dc–dc converter current stress. However, it is difficult to regulate the voltage ripples and current stress flexibly and accurately under any load condition just by the offline design of control bandwidth in the conventional method [9]. In order to absorb the double-line-frequency power, some methods add additional components. In [10], the passive magnetic components *L*–*C* are utilized to bypass the double-line-frequency power in dc bus. In [11], the active decoupling circuit is utilized to absorb the double-line-frequency power. These two methods can reduce the voltage ripple and current stress significantly at the cost of additional components and lower power density. Therefore, various control methods of double-line-frequency power in dc/dc converter have been developed to achieve different control objectives without any additional component.

A lot of methods have been developed to suppress the low-frequency fluctuations in the dc bus voltage of the two-stage single-phase converter system. Many pieces of literature focus on the reduction of dc bus voltage ripple in either LVdc side or HVdc side [12]. In [13] and [14], the dc bus voltage ripple in HVdc side is suppressed by proportional–resonant (PR) controller. In [15], the double-line-frequency power in HVdc side is compensated to the output power of DAB by feedforward method. In [16], the double-line-frequency power in HVdc side is estimated and compensated by a disturbance observer. By these methods [13], [14], [15], [16], all the double-line-frequency powers in HVdc side are transferred to LVdc side by dc/dc converter. Therefore, the dc bus voltage ripple in HVdc side can be eliminated and the capacitor in HVdc side can be reduced a lot. On the contrary, in [17] and [18], the dc bus voltage ripple in LVdc side is suppressed by the ripple voltage feedforward method. In [19], the proportional–integral–resonant controller is employed to suppress the double-line-frequency fluctuation in LVdc dc bus voltage. By these methods [17], [18], [19], all the double-line-frequency powers in LVdc side are transferred to HVdc side by the dc/dc converter. Therefore, the dc bus voltage ripple in LVdc side can be eliminated and the capacitor in LVdc side can be reduced a lot. However, these methods above can only mitigate the voltage ripple in just one side. Different from this, some methods are developed to mitigate the voltage ripple in both sides. In [12], [20], and [21], the three symmetrical single-phase double-line-frequency power, which is transferred from HVdc to LVdc by DAB, has been naturally counteracted at the common dc bus in LVdc side. Therefore, the voltage ripples in both HVdc side and LVdc side can be mitigated. However, these methods can only be employed in the three-phase structure. In [6], [22], and [23], the load inverter in LVdc side has also participated in the regulation of double-line-frequency power. The double-line-frequency power, which is transferred by DAB from HVdc to LVdc, is counteracted by the instantaneous power of the load inverter in LVdc side. Therefore, the voltage ripples in both sides can be mitigated. However, by this method, the voltage ripples in both sides can only be eliminated under strict conditions of the phase and amplitude of the instantaneous power in the LVdc load side. In most working conditions, the voltage ripples in both sides cannot be eliminated to zero by [6], [22], and [23].

It can be seen in these methods above that in order to suppress the low-frequency ripples in the dc bus voltage, the dc/dc converter has to transfer a large amount of double-line-frequency power from one side to the other. It will bring about violent double-line-frequency fluctuation in the current of dc/dc converter and lead to large current stress of dc/dc converter [24]. The low-frequency fluctuations in current will decrease the energy conversion efficiency of dc/dc converter. To solve this problem, a number of methods have been developed to suppress the low-frequency fluctuations in the current of the dc/dc converter.

In [24], [25], and [26], the input/output impedance of buck/boost-derived dc/dc converter is reshaped at a double line frequency to suppress the low-frequency fluctuations in the input/output current of dc/dc converter. However, the current through the high-frequency transformer in the isolated bidirectional dc/dc converter, e.g., DAB and *LLC*, is much different from the input/output current in the buck/boost-derived dc/dc. The methods in [24], [25], and [26] may not be effective for the reduction of high-frequency-link current stress in DAB. In [27], the high-frequency resonant current envelope ripple in *LLC* converter is suppressed by the PR controller. However, additional sensor is needed for the AD sample of high-frequency current. In [28], the high-frequency resonant current envelope ripple in SRC converter is suppressed by the third-order harmonic voltage injection without any additional device. However, the suppression effect is limited by the maximum modulation index of H-bridge rectifier. In fact, the high-frequency current in DAB is much more complicated to be solved than that in *LLC*. In previous work [29], an analytic solution is presented for minimizing the high-frequency current envelope ripple in DAB. However, the method is very sophisticated.

It is worth noting that all these control methods above [12], [13], [14], [15], [16], [17], [18], [19], [20], [21], [22], [23], [24], [25], [26], [27], [28], [29] can only achieve one optimal objective, i.e., either minimum voltage ripple or minimum current stress. However, if the smaller voltage ripple (or current stress) is achieved, the larger current stress (or voltage ripple) will be obtained. In some cases [13], [14], [15], [16], [17], [18], [19], [20], [21], [22], [23], small voltage ripple is expected to reduce bulky capacitors and improve the power quality in load side and grid side. In other cases [24], [25], [26], [27], [28], [29], small current stress is expected to improve working efficiency and increase the life span of devices. In order to adapt various working conditions and application requirements, the tradeoff [8] between voltage ripple and current stress should be made.

In this article, a double-line-frequency power control method of DAB is proposed in the two-stage single-phase system to achieve optimization and tradeoff between the current stress of DAB and the dc bus voltage ripples in both sides. Unlike the traditional methods [12], [13], [14], [15], [16], [17], [18], [19], [20], [21], [22], [23], [24], [25], [26], [27], [28], [29], the proposed methods not only take the voltage ripples in both sides into account for optimization but also achieve the optimization of DAB current stress and the flexible tradeoff between the current stress and the voltage ripples based on the optimal control trajectory (OCT). First, the optimization effects of the conventional control objectives for voltage ripples and current stress are analyzed. The OCT is proposed to achieve minimum current stress under any certain amplitude of voltage ripple. Then, the control combinations of the double-line-frequency power of OCT are derived by analytical expressions with some approximations and simplifications. The optimization effects of the approximate OCT (AOCT) are also analyzed. Next, two tradeoff control methods weighted optimal control method in AOCT (WOCT) and constrained optimal control method in AOCT (COCT) are presented to achieve flexible regulation between voltage ripple and current stress under any load condition. An optimized control scheme of the initial phase of the single-phase ac load is also derived to maximize the adjustable range of voltage ripple. Finally, the experimental results by a downscaled prototype verify the correctness and validity of the proposed OCT and the control methods.

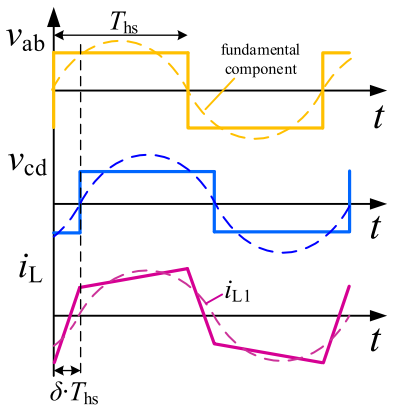

Fig. 2. Waveforms of voltage and current under SPS in DAB.

The rest of this article is organized as follows. In Section II, the double-line-frequency fluctuations in the two-stage single-phase system are derived. In Section III, the OCT is proposed and the approximate analytical calculation method is derived. In Section IV, two tradeoff control methods for voltage ripple and current stress are presented. In Section V, the feasibility and effectiveness of the proposed OCT and control methods are verified by experimental results. Finally, Section VI concludes this article.

II. Double-Line-Frequency Fluctuations in Two-Stage Single-Phase Converter System

A. Topology

The two-stage single-phase ac/dc converter system is shown in Fig. 1. The inductance L, which is reflected to the HVdc side, denotes the equivalent leakage inductance of transformer T. The current through the leakage inductance L is i_L. The dc bus on HVdc (or LVdc) side is called HVB (or LVB). The dc voltages in HVB and LVB are v_1 and v_2, respectively. C_1 and C_2 are the dc bus capacitances in HVB and LVB, respectively. i_{22} and i_{11} are the input current and output current of DAB. i_{21} is the dc output current of H-bridge rectifier. i_{12} is the load current in LVB. The turns ratio n of transformer T is set to 1 so that the analysis can be simplified. When $n \neq 1$, the analysis methods and conclusions are similar to the situation when $n = 1$. v_{s2} and i_{s2} are the ac voltage and current of grid-connection H-bridge in HVdc side. v_{s1} and i_{s1} are the voltage and current of H-bridge inverter in LVdc side for single-phase ac load. $P_{\mathrm{load,dc}}$ is the dc power of pure dc load. The reference positive directions of voltages and currents have been marked in Fig. 1.

B. Fundamental Component Analysis (FCA) of Single-Phase-Shift (SPS) Modulation in DAB

SPS is the simplest and most widely used modulation strategy of DAB. The working waveforms of DAB converter under SPS are shown in Fig. 2. T_s is the switching period of DAB. $\delta \cdot T_{\mathrm{hs}}$ is the phase-shift time between v_{ab} and v_{cd}, where T_{hs} is the half switching period of DAB and δ is the phase-shift ratio between v_{ab} and v_{cd}. In [30], the FCA is carried out to simplify the analytic forms of DAB current and power.

By the FCA method, the average output power and leakage inductance current in one switching period are

$$p_{\mathrm{DAB}} = \frac{8 v_2 v_1 \sin(\pi\delta)}{\pi^2 \omega_s L} \tag{1}$$

$$i_{L1} = \frac{4}{\pi \omega_s L}\sqrt{v_2^2 + v_1^2 - 2v_1 v_2 \cos(\pi\delta)}\sin\left(\omega_s t + \arctan\frac{A}{B}\right) \tag{2}$$

where i_{L1} is the fundamental component of i_L in one switching period, $t \in [kT_s, (k+1)T_s]$, $k = 1,2,3,\ldots$, $A = v_1\cos(\pi\delta) - v_2$, $B = v_1\sin(\pi\delta)$, $\omega_s = 2\pi f_s$, and $f_s = 1/T_s$.

C. Fluctuation Characteristics of DC Bus Voltage in HVB

The instantaneous power p_{s2} in the grid-connection H-bridge rectifier is

$$\begin{aligned} p_{s2} &= v_{s2} i_{s2} = \sqrt{2} U_{s2}\sin(\omega t)\cdot\sqrt{2} I_{s2}\sin(\omega t + \varphi_2) \\ &= U_{s2} I_{s2}\cos(\varphi_2) - U_{s2} I_{s2}\cos(2\omega t + \varphi_2) \end{aligned} \tag{3}$$

where U_{s2} and I_{s2} are the root-mean-square (RMS) values of v_{s2} and i_{s2}. $\omega = 2\pi f$ is the angular frequency of grid voltage v_g. f is 50 Hz in this article. φ_2 is the initial phase of i_{s2}.

The double-line-frequency components contribute most to the low-frequency ripples in voltage and current so that the components higher than second harmonic will be neglected in the following analysis. Under steady-state conditions, the following variables can be formulated as:

DC bus voltage in HVB

$$v_2 = V_{2,\mathrm{ref}} + v_{2,f} \text{ and } v_{2,f} = V_{2,f}\sin(2\omega t + \theta_2) \tag{4}$$

where the steady-state dc component is equal to its reference value $V_{2,\mathrm{ref}}$. The double-line-frequency fluctuation component in steady state is $v_{2,f}$. $V_{2,f}$ is the amplitude of $v_{2,f}$. θ_2 is the initial phase of $v_{2,f}$.

The instantaneous power in DAB from HVB to LVB

$$\begin{aligned} p_{\mathrm{DAB}} &= v_2 i_{22} = v_1 i_{11} \\ &= P_{\mathrm{DAB,dc}} + p_{\mathrm{DAB},f} \text{ and } p_{\mathrm{DAB},f} = P_{\mathrm{DAB},f}\sin(2\omega t + \gamma) \end{aligned} \tag{5}$$

where $P_{\mathrm{DAB,dc}}$ is the dc power in steady state, $p_{\mathrm{DAB},f}$ is the double-line-frequency fluctuation power in steady state. γ is the initial phase of $p_{\mathrm{DAB},f}$. $P_{\mathrm{DAB},f}$ is the amplitude of $p_{\mathrm{DAB},f}$. The power losses are neglected.

The mathematical model in HVB is

$$p_{s2} = v_2 i_{21} = v_2 i_{22} + v_2 C_2 \frac{dv_2}{dt}. \tag{6}$$

Substituting (3)–(5) into (6), the double-line-frequency voltage ripple $v_{2,f}$ can be solved out

$$V_{2,f} = \sqrt{\frac{U_{s2}^2 I_{s2}^2 + P_{\mathrm{DAB},f}^2 + 2U_{s2} I_{s2} P_{\mathrm{DAB},f}\sin(\gamma - \varphi_2)}{4\omega^2 C_2^2 V_{2,\mathrm{ref}}^2}} \tag{7}$$

where the phase angle θ_2 of $v_{2,f}$ can be calculated by

$$\cos(\theta_2) = \frac{-U_{s2}I_{s2}\cos(\varphi_2) - P_{\mathrm{DAB},f}\sin(\gamma)}{2\omega C_2 V_{2,f} V_{2,\mathrm{ref}}}$$
$$\sin(\theta_2) = \frac{P_{\mathrm{DAB},f}\cos(\gamma) - U_{s2}I_{s2}\sin(\varphi_2)}{2\omega C_2 V_{2,f} V_{2,\mathrm{ref}}}.$$

D. Fluctuation Characteristics of DC Bus Voltage in LVB

Two types of load that are connected to LVB can be classified. One is the pure dc power load ($P_{\mathrm{load,dc}}$), and the other is the single-phase ac load (p_{s1}). The symmetrical three-phase ac load can be categorized as a pure dc power load. Both the unbalanced three-phase ac load [19] and resistive load can be equivalent to the combination of the two types.

p_{s1} is the instantaneous power of the single-phase ac load

$$\begin{aligned} p_{s1} &= v_{s1}i_{s1} = \sqrt{2}U_{s1}\sin(\omega t+\varphi_{10})\cdot\sqrt{2}I_{s1}\sin(\omega t+\varphi_{10}+\varphi_1) \\ &= U_{s1}I_{s1}\cos(\varphi_1) - U_{s1}I_{s1}\cos(2\omega t+2\varphi_{10}+\varphi_1) \end{aligned} \tag{8}$$

where U_{s1} and I_{s1} are the RMS value of v_{s1} and i_{s1}. φ_{10} is the initial phase of v_{s1}, and φ_1 is the power factor angle of the single-phase ac load.

The dc bus voltage in LVB can be formulated as follows:

$$v_1 = V_{1,\mathrm{ref}} + v_{1,f} \text{ and } v_{1,f} = V_{1,f}\sin(2\omega t + \theta_1) \tag{9}$$

where the steady-state dc component is equal to its reference value $V_{1,\mathrm{ref}}$. The double-line-frequency fluctuation component in steady state is $v_{1,f}$. $V_{1,f}$ is the amplitude of $v_{1,f}$. θ_1 is the initial phase of $v_{1,f}$.

The mathematical model in LVB is

$$P_{\mathrm{load,dc}} + p_{s1} = v_1 i_{12} = v_1 i_{11} - v_1 C_1 \frac{dv_1}{dt}. \tag{10}$$

Substituting (5), (8), and (9) into (10), the double-line-frequency ripple in LVB voltage can be solved out

$$V_{1,f} = \sqrt{\frac{U_{s1}^2 I_{s1}^2 + P_{\mathrm{DAB},f}^2 + 2U_{s1}I_{s1}P_{\mathrm{DAB},f}\sin(\gamma-\varphi_1-2\varphi_{10})}{4\omega^2 C_1^2 V_{1,\mathrm{ref}}^2}} \tag{11}$$

where the phase angle θ_1 of $v_{1,f}$ can be calculated by

$$\cos(\theta_1) = \frac{P_{\mathrm{DAB},f}\sin(\gamma) + U_{s1}I_{s1}\cos(2\varphi_{10}+\varphi_1)}{2\omega C_1 V_{1,f} V_{1,\mathrm{ref}}}$$
$$\sin(\theta_1) = \frac{U_{s1}I_{s1}\sin(2\varphi_{10}+\varphi_1) - P_{\mathrm{DAB},f}\cos(\gamma)}{2\omega C_1 V_{1,f} V_{1,\mathrm{ref}}}.$$

E. Double-Line-Frequency Fluctuation in DAB Current Stress

According to (2), the amplitude of i_{L1}, i.e., $i_{L1,\mathrm{amp}}$, is the current stress of DAB during one switching period (fundamental component approximation). The switching frequency f_s (20 kHz) is much larger than the double line frequency (100 Hz) so that $i_{L1,\mathrm{amp}}$ can be regarded as a continuous function with time t

$$i_{L1,\mathrm{amp}}(t) = \frac{4}{\pi\omega_0 L}\sqrt{v_2^2(t) + v_1^2(t) - 2v_1(t)v_2(t)\cos(\pi\delta(t))}. \tag{12}$$

As can be seen in (1), (4), (5), and (9), v_1, v_2, and δ all fluctuate at double line frequency. Therefore, $i_{L1,\mathrm{amp}}(t)$ also fluctuates periodically at double line frequency, i.e., the envelope ripple of i_L in [27], [28], and [29], leading to the obvious increase in the current stress of DAB.

The current stress of DAB, i.e., $i_{L,\mathrm{peak}}$, is the maximum value of $i_{L1,\mathrm{amp}}(t)$ during a double-line-frequency period

$$i_{L,\mathrm{peak}} = \max_{t\in[t_0,t_0+1/(2f)]} i_{L1,\mathrm{amp}}(t). \tag{13}$$

III. OCT of DAB Current Stress and DC Bus Voltage Ripple

A. Optimal Control Trajectory

According to (7), (11), and (12), it is worth noting that $P_{\mathrm{DAB},f}$ and γ are the two controllable variables in DAB, which can be utilized to adjust the double-line-frequency fluctuations in both dc bus voltage and DAB current stress. There are various combinations of $P_{\mathrm{DAB},f}$ and γ to achieve different optimization objectives.

1) Objectives 1 and 2 are the traditional control objectives to reduce voltage ripples in single-phase two-stage system so that the bulk dc bus capacitors in HVB or LVB can be reduced a lot [12]. However, only the voltage ripple and capacitor in just one side (LVB or HVB) can be reduced. The double-line-frequency power is still transferred from one side to the other so that the maximum voltage ripple and the total capacitance in both sides may not be reduced.
   Objective 1 (HVRM): Minimum voltage ripple in HVB. In this case, DAB transfers all the double-line-frequency powers from HVB to LVB, i.e., $V_{2,f} = 0$ and $V_{1,f} \neq 0$.
   Objective 2 (LVRM): Minimum voltage ripple in LVB. In this case, DAB transfers all the double-line-frequency powers from LVB to HVB, i.e., $V_{1,f} = 0$ and $V_{2,f} \neq 0$.
2) To solve the problems above, objectives 3 and 4 are constructed as below to reduce voltage ripples on both sides.
   Objective 3 (GVRM): Global minimum voltage ripple in both sides. In this case, the maximum voltage ripples in both sides are minimized, i.e., to minimize $V_{f,\max}$ ($V_{f,\max} = \max(V_{1,f}, V_{2,f})$).
   Objective 4 (VRE): Equal voltage ripple in both sides. In this case, the double-line-frequency power in the whole system is redistributed between LVB and HVB by DAB to always make equal voltage ripples in both sides, i.e., $V_{f,\max} = V_{1,f} = V_{2,f}$.
   Objectives 1–4 are aiming at the reduction of voltage ripple and dc bus capacitances regardless of DAB current stress. However, a large amount of double-line-frequency power is transferred by DAB under these objectives. It leads to significant increase in the current stress of DAB. Different from this, objective 5 is aiming at minimizing the

TABLE I
MAIN PARAMETERS

Parameters	Nominal Value
Grid Voltage RMS Value U_g	60 V
Gird Voltage Frequency f	50 Hz
DC-Bus Capacitance C_1	420 μF
DC-Bus Capacitance C_2	420 μF
Turn Ratio n	1
Inductance L	63 μF
Switching Frequency of DAB f_s	20 kHz
DC Voltage Reference Value $V_{1,\mathrm{ref}}$	100 V
DC Voltage Reference Value $V_{2,\mathrm{ref}}$	100 V

current stress of DAB under double-line-frequency power fluctuation.

3) Objective 5 (GCSM) [29]: Global minimum current stress in DAB. In this case, $P_{\mathrm{DAB},f}$ and γ are controlled to achieve global minimum DAB current stress regardless of dc bus voltage ripple $V_{f,\max}$, i.e., to minimize $i_{L,\mathrm{peak}}$. However, these objectives above aim at the reduction of either voltage ripple or current stress. If the voltage ripple has been reduced to minimum, the current stress will be high, and vice-versa. Therefore, objective 6 is proposed in this article to allow the coordinated optimization and tradeoff between voltage ripple and current stress as follows.
4) Objective 6 (OCT): OCT of current stress and voltage ripple. In this case, $P_{\mathrm{DAB},f}$ and γ are controlled to always achieve minimum current stress of DAB under any certain value of $V_{f,\max}(=\max(V_{1,f}, V_{2,f}))$. In OCT, $V_{f,\max}$ becomes an adjustable variable and $i_{L,\mathrm{peak}}$ reaches its minimum value under any given $V_{f,\max}$. Therefore, the tradeoff between voltage ripple $V_{f,\max}$ and current stress $i_{L,\mathrm{peak}}$ can be made in OCT.

Case 1–Case 3 are listed in the following text to cover three basic load conditions in LVB. Case 4 is the hybrid load condition. Other circuit parameters are listed in Table I.

Case 1: (unity power factor load) $U_{s1} = 60$ V, $I_{s1} = 8.33$ A, $\varphi_1 = 0^\circ$, $P_{\mathrm{load,dc}} = 0$ W, and $\varphi_{10} = \varphi_2 = 0^\circ$.
Case 2: (pure reactive power load) $U_{s1} = 60$ V, $I_{s1} = 8.33$ A, $\varphi_1 = 90^\circ$, $P_{\mathrm{load,dc}} = 0$W, and $\varphi_{10} = \varphi_2 = 0^\circ$.
Case 3: (pure dc power load) $U_{s1} = 0$ V, $I_{s1} = 0$ A, $\varphi_1 = 0^\circ$, $P_{\mathrm{load,dc}} = 500$ W, and $\varphi_{10} = \varphi_2 = 0^\circ$.
Case 4: (hybrid power load) $U_{s1} = 60$ V, $I_{s1} = 8.33$ A, $\varphi_1 = 60^\circ$, $P_{\mathrm{load,dc}} = 100$ W, and $\varphi_{10} = \varphi_2 = 0^\circ$.

The $i_{L,\mathrm{peak}}$ and $V_{f,\max}$ are plotted in Fig. 3 under objectives 1–6 and Case 1–4. The $i_{L,\mathrm{peak}}$ and $V_{f,\max}$ are solved by numerical calculation of (7), (11), (12), and (13) directly with the help of MATLAB.

As shown in Fig. 3(a), every working point has a unique control combination of $P_{\mathrm{DAB},f}$ and γ. L_1–L_3 are the working points when $V_{f,\max} = 18$ V, 14 V, and 10 V, respectively. It can be seen that there are various control combinations of $P_{\mathrm{DAB},f}$ and γ corresponding to a certain $V_{f,\max}$. The $i_{L,\mathrm{peak}}$ of L_1–L_3 is plotted in Fig. 3(b). It can be seen that the $i_{L,\mathrm{peak}}$ varies with different control combinations of $P_{\mathrm{DAB},f}$ and γ at the given $V_{f,\max}$. The

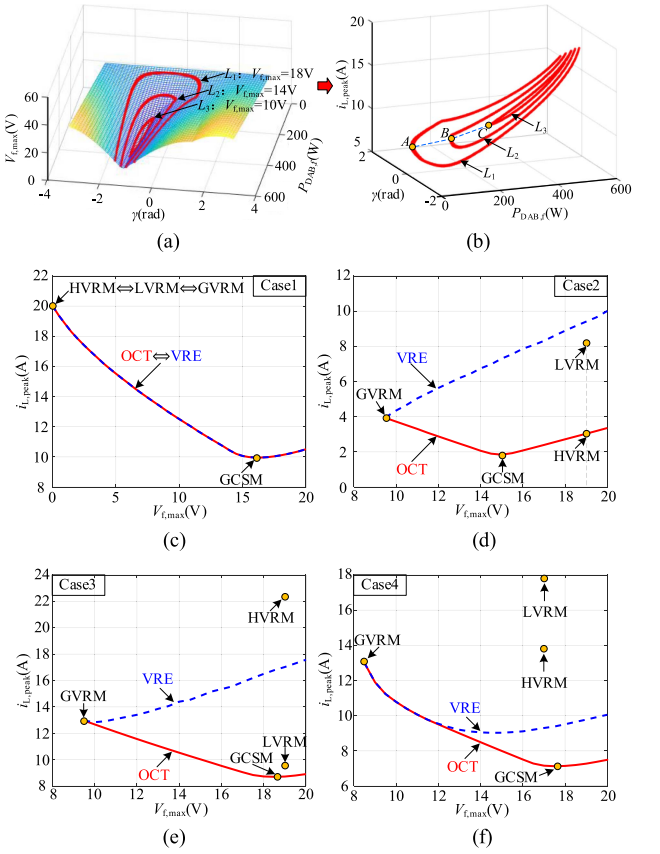

Fig. 3. $i_{L,\mathrm{peak}}$ and $V_{f,\max}$ under objective1–6 and different load conditions. (a) Three-dimensional $V_{f,\max}$ versus $P_{\mathrm{DAB},f}$ and γ in case 4. (b) Three-dimensional $i_{L,\mathrm{peak}}$ versus $P_{\mathrm{DAB},f}$ and γ of L_1–L_3. (c)–(f) Two-dimensional $i_{L,\mathrm{peak}}$ versus $V_{f,\max}$ in case 1–4, respectively.

A, B, and C in Fig. 3(b) are the only optimal working points with minimum $i_{L,\mathrm{peak}}$ when $V_{f,\max} = 18$ V, 14 V, and 10 V, respectively. The OCT consists of all these optimal working points under different given $V_{f,\max}$.

As shown in Fig. 3(c)–(f), HVRM, LVRM, GVRM, and GCSM are all corresponding to a sole working point. GVRM always has larger current stress $i_{L,\mathrm{peak}}$ than that in GCSM, while GCSM always has larger voltage ripple $V_{f,\max}$ than that in GVRM. In Case 1, HVRM, LVRM, and GVRM are equivalent working points. In Case 2, HVRM is superior to LVRM with smaller $i_{L,\mathrm{peak}}$. In Case 3, LVRM is superior to HVRM with smaller $i_{L,\mathrm{peak}}$. That is to say, LVRM and HVRM can only adapt to specific load conditions. All these objectives corresponding to fixed working points. It means that these objectives cannot achieve flexible optimization and tradeoff between current stress and voltage ripple.

Different from this, both OCT and VRE are not just a sole working point but a trajectory, as shown in Fig. 3(c)–(f). Therefore, various working points can be found in the trajectory to deal with various load conditions. GVRM and GCSM can be regarded as the start point and the end point in OCT, respectively. An infinite number of trajectories can be found between the point GVRM and the point GCSM. According to the definition of OCT, the OCT always has minimum $i_{L,\mathrm{peak}}$ under

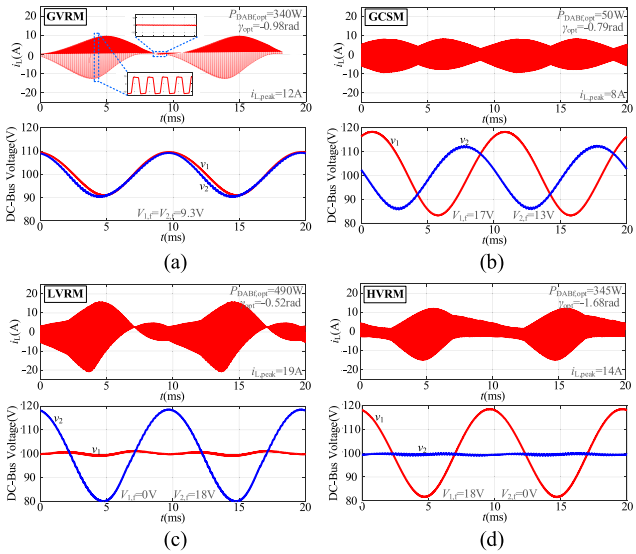

Fig. 4. Simulation waveforms in case 4 under different optimization objectives. (a) GVRM. (b) GCSM. (c) LVRM. (d) HVRM.

any certain $V_{f,\max}$. It means that the OCT will bring about higher working efficiency than other trajectories. The OCT is the best control trajectory. Moreover, OCT is a monotonically decreasing trajectory between GVRM and GCSM. As a result, the tradeoff and optimization between $i_{L,\text{peak}}$ and $V_{f,\max}$ can be made in OCT. In the right part after GCSM of OCT, the current stress will increase with the voltage ripple. Both the current stress and the voltage ripple will become worse when the working point moves right after GCSM. As a result, these working points at the right part after GCSM of OCT are neglected.

The simulation waveforms of i_L, v_1, and v_2 under different objectives in Case 4 are shown in Fig. 4. It can be seen that the envelope ripple of i_L fluctuates at double line frequency. The $i_{L,\text{peak}}$ and $V_{f,\max}$ are almost in accordance with the theoretical analysis in Fig. 3(f). The small deviation of $i_{L,\text{peak}}$ is mainly caused by the FCA method. The $V_{f,\max}$ in GVRM reaches its global minimum value and is about half of that in other objectives. The $i_{L,\text{peak}}$ in GCSM reaches its global minimum value and is much smaller than that in other objectives. It indicates that the double-line-frequency power in DAB does have obvious effects on both $i_{L,\text{peak}}$ and $V_{f,\max}$.

All working points in OCT are corresponding to an optimal control combination ($P_{\text{DAB}f,\text{opt}}$, γ_{opt}) in DAB. However, v_1, v_2, and δ in (12) all contain double-line-frequency fluctuation components, leading to extreme complexity of (12). As a result, it is very difficult to derive the accurate analytical expressions of the whole trajectory and the optimal control combination ($P_{\text{DAB}f,\text{opt}}$, γ_{opt}) directly by (12) and (13). Although OCT can be solved by offline numerical calculation and online lookup table, a large number of working parameters (U_{s1}, I_{s1}, U_{s2}, I_{s2}, φ_1, φ_2, $P_{\text{load,dc}}$, …) leads to high-dimensional lookup table. As a result, the lookup table method is also difficult to be implemented.

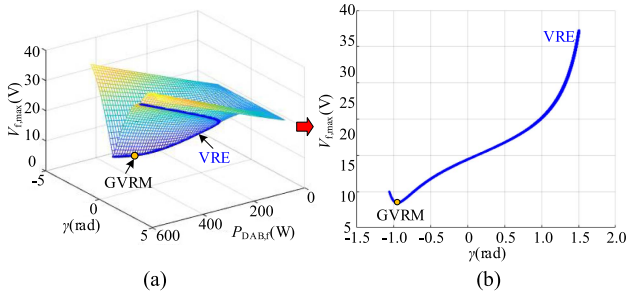

Fig. 5. $V_{f,\max}$ varied with $P_{\text{DAB},f}$ and γ. (a) Three-dimensional $V_{f,\max}$ versus $P_{\text{DAB},f}$ and γ. (b) Two-dimensional VRE trajectory $V_{f,\max}$ versus γ.

In spite of this, OCT still can be solved by analytical expressions based on some approximations and simplifications.

B. Analytical Solution of GVRM

As can be seen in Fig. 3(c)–(f), GVRM is the start point in the trajectories of both VRE and OCT. GVRM represents the best optimization result of $V_{f,\max}$. Different from OCT, $i_{L,\text{peak}}$ is not needed to be optimized in VRE. Therefore, the solution process of VRE is much simpler than that of OCT. GVRM can be derived according to VRE rather than OCT. The 3-D surface of $V_{f,\max}$ versus $P_{\text{DAB},f}$ and γ under Case 4 is plotted in Fig. 5. The trajectory of VRE is plotted as a blue solid line. The condition $V_{f,\max} = V_{1,f} = V_{2,f}$ is satisfied in every point in VRE. GVRM is the minimum point in the trajectory.

The accurate values of $P_{\text{DAB},f}|_{\text{GVRM}}$, γ_{GVRM}, and $V_{f,\max}|_{\text{GVRM}}$ at the point GVRM can be derived as analytical expressions (14)–(16) by Lagrange multiplier method

$$\begin{cases} F(P_{\text{DAB},f},\ \gamma,\ \lambda) = V_{2,f} + \lambda(V_{2,f} - V_{1,f}) \\ \dfrac{\partial F}{\partial P_{\text{DAB},f}} = 0,\ \dfrac{\partial F}{\partial \gamma} = 0,\ \dfrac{\partial F}{\partial \lambda} = 0 \end{cases}$$

$$\Rightarrow P_{\text{DAB},f}|_{\text{GVRM}} = \sqrt{\frac{k_0(U_{s1}^2 I_{s1}^2 + U_{s2}^2 I_{s2}^2 + 2U_{s1}I_{s1}U_{s2}I_{s2}\cos(\varphi_2 - \varphi_1 - 2\varphi_{10}))}{(k_0+1)^2} + (k_0-1)\frac{k_0 U_{s2}^2 I_{s2}^2 - U_{s1}^2 I_{s1}^2}{(k_0+1)^2}} \tag{14}$$

$$\gamma_{\text{GVRM}} \Leftarrow \begin{cases} \sin(\gamma_{\text{GVRM}} - \varphi_2) = -\dfrac{k_0 U_{s2} I_{s2} + U_{s1} I_{s1} cos(\varphi_2 - \varphi_1 - 2\varphi_{10})}{(k_0+1)\, P_{\text{DAB},f}|_{\text{GVRM}}} \\ \cos(\gamma_{\text{GVRM}} - \varphi_2) = -\dfrac{U_{s1} I_{s1} \sin(\varphi_2 - \varphi_1 - 2\varphi_{10})}{(k_0+1)\, P_{\text{DAB},f}|_{\text{GVRM}}} \end{cases} \tag{15}$$

$$V_{f,\max}|_{\text{GVRM}} = \frac{\sqrt{U_{s2}^2 I_{s2}^2 + U_{s1}^2 I_{s1}^2 - 2U_{s1}I_{s1}U_{s2}I_{s2}\cos(\varphi_2 - \varphi_1 - 2\varphi_{10})}}{2\omega(C_1 V_{1,\text{ref}} + C_2 V_{2,\text{ref}})} \tag{16}$$

where $k_0 = (C_1 \cdot V_{1,\text{ref}})\,/(C_2 \cdot V_{2,\text{ref}})$.

Equation (16) reveals that the C_1 and C_2 in the two-stage system can be equivalent to a capacitor C_e at the working point

GVRM. The numerator of (16) is the amplitude of the total double-line-frequency power in the system, i.e., the amplitude of $p_f = U_{s1}I_{s1}\cos(2\omega t + 2\varphi_{10} + \varphi_1) - U_{s2}I_{s2}\cos(2\omega t + \varphi_2)$ is calculated by (3) and (8). Equation (16) can be rewritten as follows:

$$V_{f,\max}|_{\mathrm{GVRM}} = \frac{P_f}{2\omega(C_1V_{1,\mathrm{ref}} + C_2V_{2,\mathrm{ref}})} = \frac{P_f}{2\omega C_eV_e} \quad (17)$$

where C_e is the equivalent capacitor in the two-stage converter system, V_e is the equivalent nominal dc voltage of C_e. $X_e = 1/(2\omega C_e)$ is the equivalent impedance of C_e at double line frequency. $I_e = P_f/V_e$ is the equivalent current of C_e at double line frequency. C_e is equivalent to the parallel connection of C_1 and C_2, i.e., $C_e = C_1 + C_2$. It means that C_1 and C_2 are fully utilized to absorb all the double-line-frequency power in the system so that the dc bus voltage ripples can be suppressed to the greatest extent. V_e is the weighted average of $V_{1,\mathrm{ref}}$ and $V_{2,\mathrm{ref}}$ according to the capacitances in LVB and HVB, i.e., $V_e = (C_1V_{1,\mathrm{ref}} + C_2V_{2,\mathrm{ref}})/(C_1 + C_2)$, V_e is always between $V_{1,\mathrm{ref}}$ and $V_{2,\mathrm{ref}}$.

In fact, the term $(C_1V_{1,\mathrm{ref}} + C_2V_{2,\mathrm{ref}})$ in (16) is the total charge storage of C_1 and C_2 under respective nominal voltage $V_{1,\mathrm{ref}}$ and $V_{2,\mathrm{ref}}$. It denotes the maximum charge that can be stored by the equivalent capacitance C_e, i.e., $Q_{\max} = C_eV_e$. Therefore, minimum voltage ripple $V_{f,\max}|_{\mathrm{GVRM}}$ is achieved by the maximum equivalent capacitance C_e at the point GVRM.

In most applications, $V_{1,\mathrm{ref}}$, $V_{2,\mathrm{ref}}$ and C_1 and C_2 are designed to match the turns ratio of transformer T so that the reactive current in DAB can be reduced [30]. Under this circumstance, $k_0 = 1$, (14) and (15) can be simplified to be

$$P_{\mathrm{DAB},f}|_{\mathrm{GVRM}} = \frac{\sqrt{U_{s1}^2I_{s1}^2 + U_{s2}^2I_{s2}^2 + 2U_{s1}I_{s1}U_{s2}I_{s2}\cos(\varphi_2 - \varphi_1 - 2\varphi_{10})}}{2}$$

$$\gamma_{\mathrm{GVRM}} = \begin{cases} \arcsin\left(-\frac{U_{s2}I_{s2}\cos(\varphi_2) + U_{s1}I_{s1}\cos(\varphi_1 + 2\varphi_{10})}{2P_{\mathrm{DAB},f}|_{\mathrm{GVRM}}}\right) \\ \arccos\left(\frac{U_{s2}I_{s2}\sin(\varphi_2) + U_{s1}I_{s1}\sin(\varphi_1 + 2\varphi_{10})}{2P_{\mathrm{DAB},f}|_{\mathrm{GVRM}}}\right). \end{cases}$$

C. Approximate Solution of GCSM

The SHCS method has been proposed in previous work [29] to solve the point GCSM of DAB with relatively high accuracy. However, the solution process is too sophisticated and only the low-frequency voltage ripple in v_2 is considered. In this article, the double-line-frequency voltage ripple exists in both v_1 and v_2, leading to much more complex solution process. The method in [29] cannot be used in this article.

Three load conditions are listed below (case 5–case 7) to cover the variation of φ_1, φ_2, and $P_{\mathrm{load,dc}}$. At the two working points GCSM and GVRM, the $i_{L,\mathrm{peak}}$, $V_{f,\max}$, and $P_{\mathrm{DAB},f}$ are plotted in Fig. 6.

Case 5: (varying power factor of 1-ph ac load) $U_{s1} = 60$ V, $I_{s1} = 8.33$ A, $\varphi_1 = -90^\circ \sim +90^\circ$, $P_{\mathrm{load,dc}} = 0$ W, and $\varphi_{10} = \varphi_2 = 0^\circ$.

Case 6: (varying power of dc load) $U_{s1} = 60$ V, $I_{s1} = 8.33$ A, $\varphi_1 = 60^\circ$, $P_{\mathrm{load,dc}} = 0$–250 W, and $\varphi_{10} = \varphi_2 = 0^\circ$.

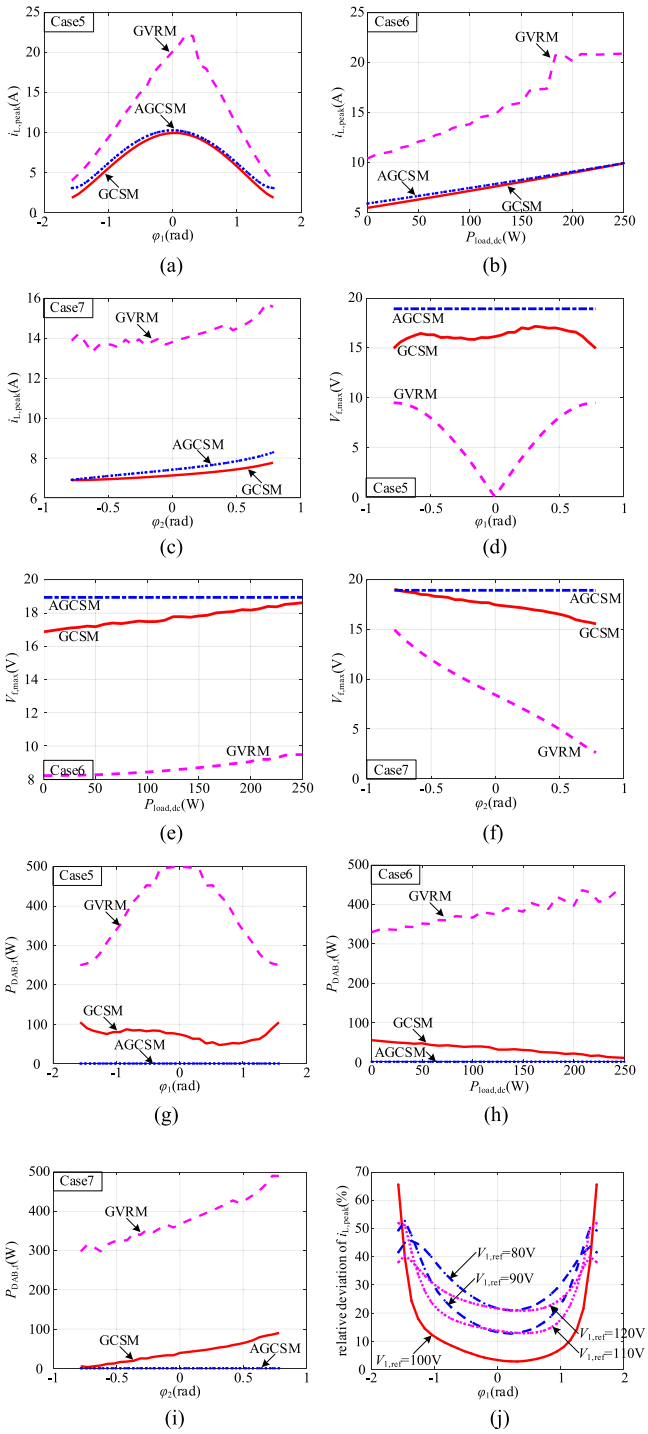

Fig. 6. $i_{L,\mathrm{peak}}$, $V_{f,\max}$, and $P_{\mathrm{DAB},f}$ at the working points GVRM, GCSM, and AGCSM in case 5–7. (a)–(c) $i_{L,\mathrm{peak}}$. (d)–(f) $V_{f,\max}$. (g)–(i) $P_{\mathrm{DAB},f}$. (j) Relative errors of $i_{L,\mathrm{peak}}$ between GCSM and AGCSM in Case 5 under different $V_{1,\mathrm{ref}}$ ($V_{2,\mathrm{ref}}$ is fixed at 100 V).

Case 7: (varying power factor in grid side) $U_{s1} = 60$ V, $I_{s1} = 8.33$ A, $\varphi_1 = 60^\circ$, $P_{\mathrm{load,dc}} = 100$ W, $\varphi_{10} = 0^\circ$, and $\varphi_2 = -45^\circ \sim +45^\circ$.

As shown in Fig. 6(a)–(c) and (g)–(i), both the $i_{L,\mathrm{peak}}$ and $P_{\mathrm{DAB},f}$ of GVRM are much larger than that of GCSM. Compared with the $P_{\mathrm{DAB},f}$ of GVRM, the $P_{\mathrm{DAB},f}$ of GCSM is much

smaller and close to zero in most of the variation ranges of φ_1, φ_2, and $P_{\mathrm{load,dc}}$. Therefore, the working point GCSM is approximated (AGCSM) by setting $P_{\mathrm{DAB},f}=0$ in this article to avoid the complex solution process. Substituting $P_{\mathrm{DAB},f}=0$ into (7) and (11) to derive the voltage ripple $V_{f,\max}$ at the point AGCSM

$$P_{\mathrm{DAB},f}|_{\mathrm{AGCSM}}=0$$
$$\Rightarrow V_{f,\max}|_{\mathrm{AGCSM}}=\max\left(\frac{U_{s1}I_{s1}}{2\omega C_1 V_{1,\mathrm{ref}}},\frac{U_{s2}I_{s2}}{2\omega C_2 V_{2,\mathrm{ref}}}\right). \quad (18)$$

In order to achieve better optimization effect of $i_{L,\mathrm{peak}}$ at AGCSM, the deviations between GCSM and AGCSM are supposed to be as small as possible. The deviations are analyzed under different cases as follows.

1) In Case 6 and Case 7: As shown in Fig. 6(b) and (c), the relative deviations of $i_{L,\mathrm{peak}}$ are smaller than 5%, which can be neglected. The variations of φ_2 and $P_{\mathrm{load,dc}}$ will not cause significant deviations of $i_{L,\mathrm{peak}}$ between GCSM and AGCSM. The optimization effect can be guaranteed in Case 6 and Case 7.
2) In Case 5: As shown in Fig. 6(a) and (j), when φ_1 is not very close to $\pm\pi/2$, the relative deviation of $i_{L,\mathrm{peak}}$ is smaller than 10%, which can be accepted. The maximum relative deviation of $i_{L,\mathrm{peak}}$ occurs when φ_1 approaches $\pm\pi/2$, i.e., Case 2. Under this circumstance, $i_{L,\mathrm{peak}}$ is very small, for the reason that almost no active power is transferred by DAB. Although the relative deviation of $i_{L,\mathrm{peak}}$ is large, the absolute deviation of $i_{L,\mathrm{peak}}$ is small. Therefore, the deviations between GCSM and AGCSM will not significantly deteriorate the working efficiency of DAB when φ_1 approaches $\pm\pi/2$. Not only that, in most practical applications, the power factor of ac load will not be very close to zero. The optimization effects can be guaranteed in Case 5.
3) It can be seen in Fig. 6(j) that the larger the deviation between $V_{1,\mathrm{ref}}$ and $V_{2,\mathrm{ref}}$, the larger the relative errors of $i_{L,\mathrm{peak}}$ between GCSM and AGCSM. The v_1 and v_2 of the two-stage system in Fig. 1 are controllable. Therefore, $V_{1,\mathrm{ref}}$ and $V_{2,\mathrm{ref}}$ are generally controlled to match the turns ratio n of T [30] so that the reactive circulating current of DAB can be reduced. Even if $V_{1,\mathrm{ref}}$ deviates from $V_{2,\mathrm{ref}}$ slightly, the relative deviations of $i_{L,\mathrm{peak}}$ between GCSM and AGCSM are smaller than 20% as long as φ_1 does not approach $\pm\pi/2$. As long as $V_{1,\mathrm{ref}}$ does not deviate from $V_{2,\mathrm{ref}}/n$ too much, the optimization effect can be guaranteed.

To sum up, the optimization effect still can be guaranteed even if the GCSM is approximated by the AGCSM.

D. Approximate Solution of OCT

The $P_{\mathrm{DAB}f,\mathrm{opt}}$ and γ_{opt} of OCT under Case 1–Case 4 are plotted in Fig. 7. $P_{\mathrm{DAB}f,\mathrm{opt}}$ exhibits good linear relation with $V_{f,\max}$, especially in Case 1 and Case 2. Therefore, $P_{\mathrm{DAB}f,\mathrm{opt}}$

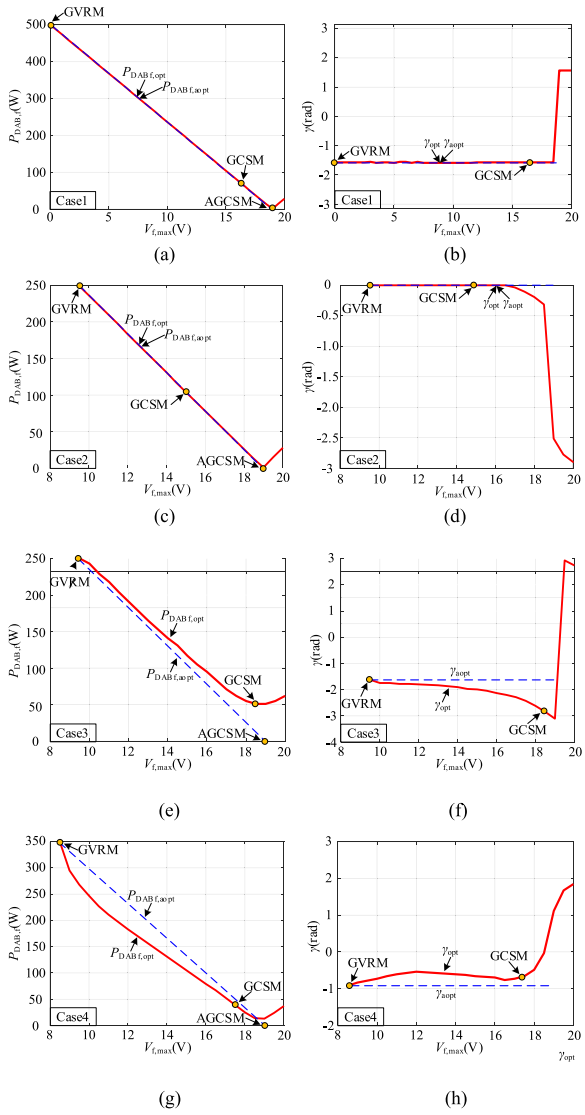

Fig. 7. Optimal values (solid line) and approximate values (dashed line) of $P_{\mathrm{DAB},f}$ and γ in (a) and (b) case 1, (c) and (d) case 2, (e) and (f) case 3, and (g) and (h) case 4.

is calculated by linear approximation as follows:

$$P_{\mathrm{DAB}f,a\mathrm{opt}}(V_{f,\mathrm{set}})=\frac{-V_{f,\mathrm{set}}+V_{f,\max}|_{\mathrm{AGCSM}}}{V_{f,\max}|_{\mathrm{AGCSM}}-V_{f,\max}|_{\mathrm{GVRM}}}\cdot P_{\mathrm{DAB},f}|_{\mathrm{GVRM}} \quad (19)$$

where $V_{f,\mathrm{set}}$ is the expected value of $V_{f,\max}$, $P_{\mathrm{DAB}f,a\mathrm{opt}}$ is the linear approximation of $P_{\mathrm{DAB}f,\mathrm{opt}}$, and $V_{f,\mathrm{set}}$ is in the range of $[V_{f,\max}|_{\mathrm{GVRM}}, V_{f,\max}|_{\mathrm{AGCSM}}]$.

Six working points in OCT are marked in Fig. 8 as P_1–P_6. In Fig. 8(a), only the control parameter γ of P_1–P_6 deviates $\pm30\%$ from its optimal value γ_{opt}, i.e., γ varies from $0.7\gamma_{\mathrm{opt}}$ to $1.3\gamma_{\mathrm{opt}}$ and $P_{\mathrm{DAB},f}=P_{\mathrm{DAB}f,\mathrm{opt}}$. In Fig. 8(b), only the control parameter $P_{\mathrm{DAB},f}$ of P_1 and P_4–P_6 deviates $\pm20\%$ from its optimal value $P_{\mathrm{DAB}f,\mathrm{opt}}$, i.e., $P_{\mathrm{DAB},f}$ varies from $0.8P_{\mathrm{DAB},f,\mathrm{opt}}$ to $1.2P_{\mathrm{DAB},f,\mathrm{opt}}$ and $\gamma=\gamma_{\mathrm{opt}}$. Under the variations of $P_{\mathrm{DAB},f}$

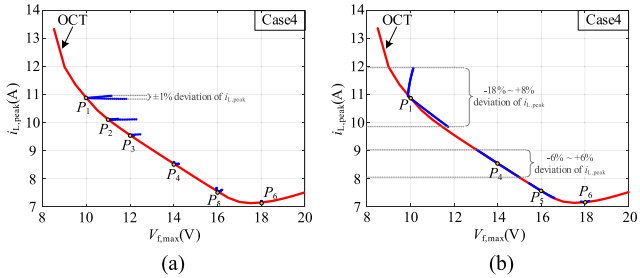

Fig. 8. Parameters sensitivity of the working points in OCT (case 4) to (a) γ and (b) $P_{\mathrm{DAB},f}$.

and γ, the actual working points(the blue points in Fig. 8 around P_1–P_6) will deviate from the ideal optimal working points P_1–P_6.

The parameter sensitivity of the working points in OCT to $P_{\mathrm{DAB},f}$ or γ is analyzed as follows.

1) As shown in Fig. 8(a), the variation of γ almost has no effect on the value of $i_{L,\mathrm{peak}}$. It indicates that $i_{L,\mathrm{peak}}$ is not sensitive to the variation of γ.
2) As shown in Fig. 8(b), the variation of $P_{\mathrm{DAB},f}$ leads to significant deviations in $i_{L,\mathrm{peak}}$. It indicates that the working points in OCT are very sensitive to the variation of $P_{\mathrm{DAB},f}$.
3) As shown in Fig. 8(a), the influence of the variation of γ on $i_{L,\mathrm{peak}}$ and $V_{f,\max}$ decreases rapidly as the working point moves to GCSM.

In Case 1 and Case 2, as shown in Fig. 7(b) and (d), γ_{opt} can be regarded as a constant γ_{GVRM} between GVRM and GCSM. In Case 3, as shown in Fig. 7(f), the deviation between γ_{opt} and γ_{GVRM} is small when $V_{f,\max}$ is small. Although the deviation between γ_{opt} and γ_{GVRM} becomes larger when the working point moves to GCSM, the influence of the variation of γ on the working points is still small, according to analysis 3) above. Therefore, γ_{opt} still can be approximated as a constant γ_{GVRM} under the pure dc power load type.

Based on the analysis above, γ_{opt} is approximated as a constant in this article

$$\gamma_{a\mathrm{opt}} = \gamma_{\mathrm{GVRM}}. \tag{20}$$

A new control trajectory, which is called AOCT, is formed based on the control combinations $P_{\mathrm{DAB}f,a\mathrm{opt}}$ and $\gamma_{a\mathrm{opt}}$ by (19) and (20). The OCT and AOCT in Case 1–Case 4 are plotted in Fig. 9.

E. Comparison of OCT With AOCT

Different from the $P_{\mathrm{DAB}f,\mathrm{opt}}$ and γ_{opt} of OCT, the $P_{\mathrm{DAB}f,a\mathrm{opt}}$ and $\gamma_{a\mathrm{opt}}$ of AOCT can be calculated by simple analytical expressions (19) and (20). As a result, not only the high-dimensional lookup table can be avoided but also the high-speed calculation can be achieved.

In Case 1 and Case 2, as shown in Fig. 7(a)–(d), the $P_{\mathrm{DAB}f,a\mathrm{opt}}$–$V_{f,\max}$ line coincides with the $P_{\mathrm{DAB}f,\mathrm{opt}}$-$V_{f,\max}$ line; the $\gamma_{a\mathrm{opt}}$ and γ_{opt} are approximated to be the same constant. Therefore, in Case 1, the trajectory of AOCT coincides with the trajectory of OCT, as shown in Fig. 9(a). However, in Case 2, the deviation between GCSM and AGCSM reaches its maximum value, as analyzed in Section III-C. As a result, in Case 2, the trajectory of AOCT coincides with the trajectory of OCT only when $V_{f,\max}|_{\mathrm{GVRM}} \le V_{f,\max} \le V_{f,\max}|_{\mathrm{GCSM}}$, as shown in Fig. 9(b). In Case 3 and Case 4, the relative deviation of $i_{L,\mathrm{peak}}$ between OCT and AOCT is smaller than 5% in most region of the trajectories. The maximum relative deviation of $i_{L,\mathrm{peak}}$ is around 10% in both cases, as shown in Fig. 9(c) and (d). Therefore, the deviations can be acceptable in Case 3 and Case 4.

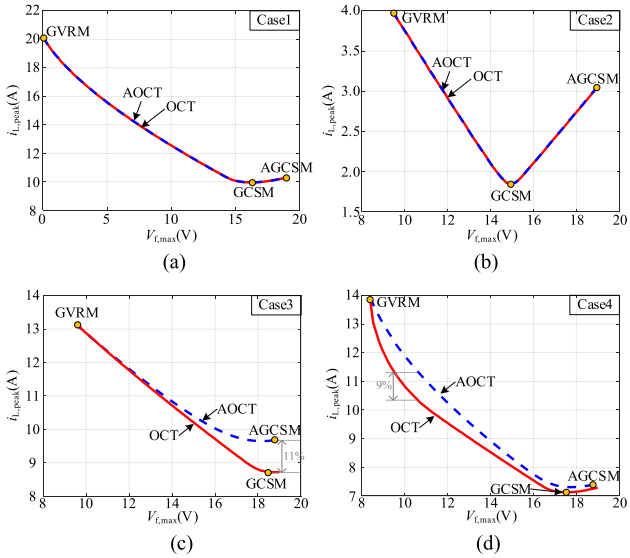

Fig. 9. OCT and AOCT in (a) case 1, (b) case 2, (c) case 3, and (d) case 4.

To sum up, AOCT is a good approximation and simplification of OCT under different load conditions and with similar optimization effects.

IV. Tradeoff in the Control of Double-Line-Frequency Power in DAB

A. Approximate Calculation of DAB Current Stress

In order to make weighted control between voltage ripple and current stress under any load condition, the DAB current stress $i_{L,\mathrm{peak}}$ is needed to be calculated in real time. Therefore, the calculation method of $i_{L,\mathrm{peak}}$ should be simple enough to reduce the computational burden in microprocessor.

However, as can be seen in [29], it is difficult to derive the analytical expressions of $i_{L,\mathrm{peak}}$ under double-line-frequency fluctuation. In this article, not only v_2 and δ but also v_1 contain double-line-frequency fluctuation components. Therefore, it is too complicated to derive the analytical expressions of $i_{L,\mathrm{peak}}$ by the method in [29].

According to (1) and (12), the key to solve the current stress of DAB is to solve the maximum value of the function $f(t)$

as follows:

$$\max_{t\in[t_0,t_0+1/(2f)]} f(t) = v_2^2(t)+v_1^2(t)-2v_1(t)v_2(t)\sqrt{1-\left(\frac{\pi^2\omega_s L p_{\mathrm{DAB}}(t)}{8v_2(t)v_1(t)}\right)^2}. \tag{21}$$

The square root term in (21) leads to great complexity when solving the maximum value of $f(t)$. Two approximations can be made as follows.

1) $V_{1,f}$ and $V_{2,f}$ are generally required to be much smaller than $V_{1,\mathrm{ref}}$ and $V_{2,\mathrm{ref}}$ to ensure the stable operation of the H-bridge rectifier and high-power quality of load. Therefore, the $v_1(t)$ and $v_2(t)$ under the square root in (21) can be approximated to its dc components $V_{1,\mathrm{ref}}$ and $V_{2,\mathrm{ref}}$.
2) Equation (21) is aiming at obtaining the maximum value of $f(t)$. Therefore, the $p_{\mathrm{DAB}}(t)$ under the square root can be zoomed in to its maximum value: $P_{\mathrm{DAB,dc}}+P_{\mathrm{DAB},f}$.

It is worth noting that only the square root term in (21) is approximated and the other terms in (21) remain unchanged. Therefore, the deviations brought by the approximations above can be reduced. Equation (21) can be simplified to be as follows:

$$\max_{t\in[t_0,t_0+1/(2f)]} f(t) = v_2^2(t)+v_1^2(t)-2k_1v_1(t)v_2(t)$$

$$k_1=\sqrt{1-\left(\frac{\pi^2\omega_s L(P_{\mathrm{DAB,dc}}+P_{\mathrm{DAB},f})}{8V_{2,\mathrm{ref}}V_{1,\mathrm{ref}}}\right)^2} \tag{22}$$

where k_1 is unrelated to time t.

Based on (4), (9), and (22), the analytical expressions of DAB current stress $i_{L,\mathrm{peak}}$ can be derived as follows:

$$i_{L,\mathrm{peak}}=\frac{4}{\pi\omega_s L}\sqrt{\begin{array}{l}V_{2,\mathrm{ref}}^2+V_{1,\mathrm{ref}}^2-2k_1V_{1,\mathrm{ref}}V_{2,\mathrm{ref}}\\+2\sqrt{A^2V_{1,f}^2+B^2V_{2,f}^2+2ABV_{1,f}V_{2,f}\cos(\theta_1-\theta_2)}\end{array}} \tag{23}$$

where $V_{1,f}$, $V_{2,f}$, θ_1, and θ_2 can be calculated by (7) and (11). $A=V_{1,\mathrm{ref}}-k_1\cdot V_{2,\mathrm{ref}}$ and $B=V_{2,\mathrm{ref}}-k_1\cdot V_{1,\mathrm{ref}}$.

If $V_{1,\mathrm{ref}}=V_{2,\mathrm{ref}}$, then (23) can be simplified to be as follows:

$$i_{L,\mathrm{peak}}=\frac{4\sqrt{2(1-k_1)}}{\pi\omega_s L}\sqrt{V_{1,\mathrm{ref}}^2+V_{1,\mathrm{ref}}\sqrt{V_{1,f}^2+V_{2,f}^2+2V_{1,f}V_{2,f}\cos(\theta_1-\theta_2)}}. \tag{24}$$

The accurate values and the approximate values of $i_{L,\mathrm{peak}}$ solved by (13) and (23), respectively, under different load conditions are plotted in Fig. 10 (Accurate values: the solid line; Approximate values: the dashed line). The maximum relative deviation (around 12%) occurs at the working point GCSM under the pure dc power load (Case 3). In all cases, the relative errors are smaller than 10% in most of the range. It indicates that $i_{L,\mathrm{peak}}$ can be approximately solved by (23) with small deviations.

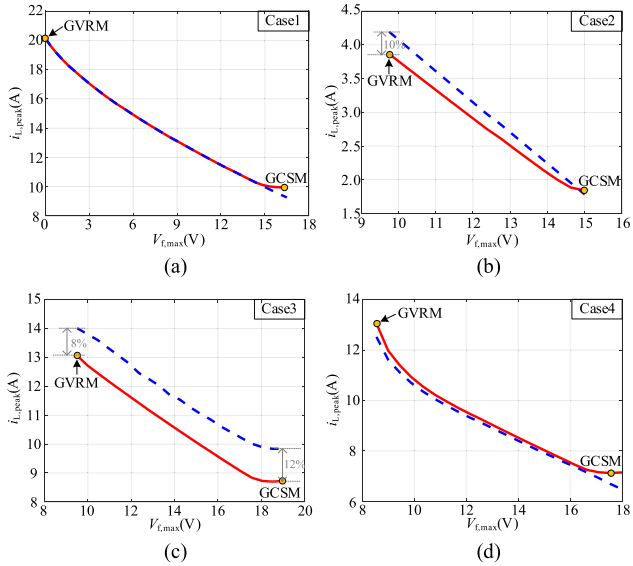

Fig. 10. Accurate values and the approximate values of $i_{L,\mathrm{peak}}$ under (a) case 1, (b) case 2, (c) case 3, and (d) case 4.

B. Weighted Control of Voltage Ripple and Current Stress in AOCT

Various weighted objective functions can be constructed to achieve different optimization effects. In this article, a quadratic weighted objective function can be constructed as (25). $i_{L,\mathrm{peak}}$ and $V_{f,\max}$ are normalized to their maximum values $i_{L,\mathrm{peak}}|_{\mathrm{GVRM}}$ and $V_{f,\max}|_{\mathrm{AGCSM}}$, respectively, so that $i_{L,\mathrm{peak}}$ and $V_{f,\max}$ can be put in one function to evaluate

$$g=\alpha\cdot\left(\frac{V_{f,\max}}{V_{f,\max}|_{\mathrm{AGCSM}}}\right)^2+(1-\alpha)\cdot\left(\frac{i_{L,\mathrm{peak}}}{i_{L,\mathrm{peak}}|_{\mathrm{GVRM}}}\right)^2+g_p \tag{25}$$

where α is the weight coefficient. The $V_{f,\max}$ and $i_{L,\mathrm{peak}}$ obey the AOCT. If $V_{f,\max}$ and $i_{L,\mathrm{peak}}$ need to be limited, then the penalty function [31] g_p can be added. If $V_{f,\max}$ and $i_{L,\mathrm{peak}}$ do not exceed their maximum allowable values $V_{f,\mathrm{lim}}$ and $i_{L\mathrm{peak,lim}}$, then $g_p=0$ and g is determined by the first two terms in (25) so that the weighted control can be done properly. If $V_{f,\max}$ and $i_{L,\mathrm{peak}}$ exceed $V_{f,\mathrm{lim}}$ and $i_{L\mathrm{peak,lim}}$, g_p becomes very large and g is mostly determined by g_p so that $V_{f,\max}$ and $i_{L,\mathrm{peak}}$ will not exceed the limits during the minimization process of objective function g. $V_{f,\max}$ and $i_{L,\mathrm{peak}}$ are limited by many factors, e.g., the tolerance capacity of devices, power quality of load, energy conversion efficiency, stable operation range, and so on.

In the conventional control method, v_1 and v_2 are generally controlled by DAB and front-end H-bridge rectifier, respectively, as shown in Fig. 11, when $p_f=0$. G_1 is the PI controller k_p+k_i/s. The double-line-frequency fluctuation in v_1 propagates into the closed-loop controller by the negative feedback path, leading to the uncontrollable double-line-frequency fluctuation in the instantaneous power of DAB.

A weighted control method of $i_{L,\mathrm{peak}}$ and $V_{f,\max}$ in AOCT (WOCT) is presented with feedforward path p_f, as shown in

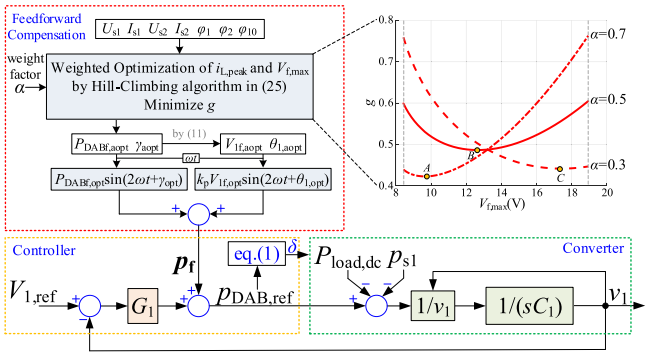

Fig. 11. Control block diagram of WOCT method in DAB.

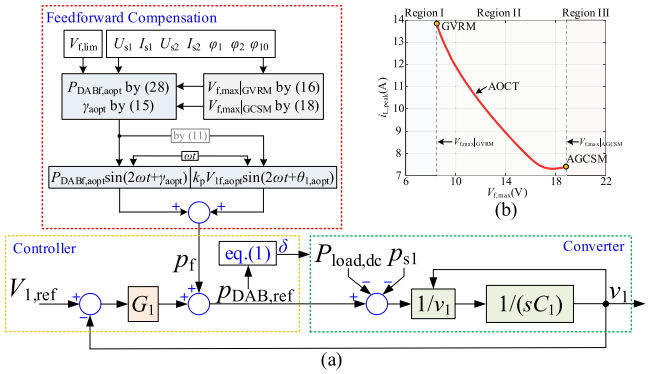

Fig. 12. COCT method in DAB. (a) Control block diagram. (b) Three regions of $V_{f,\lim}$.

Fig. 11. The double-line-frequency power of DAB is controlled in open loop through the feedforward path. Therefore, the closed-loop bandwidth and stability will not be affected by the presented control method. As shown in Fig. 11, the objective function g is a concave function with only one minimum point, which can be solved by simple hill-climbing algorithm [32]. The points A, B, and C are the minimum points of g under a different weighted factor α. The hill-climbing method (or perturb and observe method) has been widely applied to PV generation system to achieve MPPT. The detailed implementation of the hill-climbing method is not described repeatedly here. $P_{\mathrm{DAB}f,a\mathrm{opt}}$ and $\gamma_{a\mathrm{opt}}$ are the optimal control combination at the minimum point of g in AOCT. $V_{1f,a\mathrm{opt}}$ and $\theta_{1,a\mathrm{opt}}$ are the optimal values of $V_{1,f}$ and θ_1 by $P_{\mathrm{DAB}f,a\mathrm{opt}}$ and $\gamma_{a\mathrm{opt}}$.

By the WOCT method, $V_{f,\max}$ and $i_{L,\mathrm{peak}}$ can be adjusted flexibly by α to adapt different load conditions. Under steady-state conditions, $p_{\mathrm{DAB,ref}}$ can be derived as (26). Due to $kp>>ki/(2\omega)$, (26) can be simplified further

$$\begin{aligned} p_{\mathrm{DAB}f,\mathrm{ref}} &= -G_1 \cdot v_{1,f} + p_f \\ &= -V_{1f,a\mathrm{opt}}\sqrt{k_p^2+\frac{k_i^2}{4\omega^2}}\sin\left(2\omega t+\theta_{1,a\mathrm{opt}}-\arctan\left(\frac{k_i}{2\omega k_p}\right)\right) \\ &\quad + p_f \approx -k_p V_{1f,a\mathrm{opt}}\sin(2\omega t+\theta_{1,a\mathrm{opt}})+p_f. \end{aligned} \tag{26}$$

The $p_{\mathrm{DAB}f,\mathrm{ref}}$ should be equal to the optimal value $p_{\mathrm{DAB}f,a\mathrm{opt}}$. The feedforward power p_f can be derived as follows:

$$p_f = P_{\mathrm{DAB}f,a\mathrm{opt}}\sin(2\omega t+\gamma_{a\mathrm{opt}})+k_p V_{1f,a\mathrm{opt}}\sin(2\omega t+\theta_{1,a\mathrm{opt}}). \tag{27}$$

C. Minimum Current Stress Control With Voltage Ripple Constraint in AOCT

In many application scenarios, the dc voltage ripple $V_{f,\max}$ is limited strictly to its maximum allowable value $V_{f,\lim}$ so that the stable operation and the power quality of H-bridge rectifier and load can be guaranteed. Under this circumstance, the voltage ripple constrained optimal control method in AOCT (COCT) is presented, as shown in Fig. 12(a). Similar to the WOCT method, the COCT method is still based on the control structure of feedforward compensation. In COCT, voltage ripple constraint has the highest priority to be optimized, and then $i_{L,\mathrm{peak}}$ is optimized to be as small as possible to improve the working efficiency of DAB. In fact, COCT is a single-objective optimization problem with a constraint condition.

As can be seen in Fig. 12(b), $V_{f,\lim}$ may locate in three regions with regard to $V_{f,\max}$. In region I, $V_{f,\lim}$ is smaller than the global minimum voltage ripple $V_{f,\max}|_{\mathrm{GVRM}}$ so that GVRM is the nearest point to $V_{f,\lim}$. In region III, the voltage ripple in AOCT is always smaller than $V_{f,\lim}$ so that AGCSM is the optimal working point. In region II, the optimal working point is the one exactly when $V_{f,\max}=V_{f,\lim}$ so that $i_{L,\mathrm{peak}}$ is minimized when the voltage ripple constraint is met.

The optimal control combination $P_{\mathrm{DAB}f,a\mathrm{opt}}$ and $\gamma_{a\mathrm{opt}}$ can be solved by the following equation:

$$\begin{aligned} &P_{\mathrm{DAB}f,a\mathrm{opt}}(V_{f,\lim}) \\ &= \begin{cases} P_{\mathrm{DAB},f}|_{\mathrm{GVRM}}, & \text{Region } I: V_{f,\lim} < V_{f,\max}|_{\mathrm{GVRM}} \\ P_{\mathrm{DAB}f,a\mathrm{opt}}(V_{f,\lim}), & \text{Region } II: V_{f,\max}|_{\mathrm{GVRM}} \le V_{f,\lim} \\ & \le V_{f,\max}|_{\mathrm{AGCSM}} \\ 0, & \text{Region III}: V_{f,\lim} > V_{f,\max}|_{\mathrm{AGCSM}} \end{cases} \\ &\gamma_{a\mathrm{opt}} = \gamma_{\mathrm{GVRM}}. \end{aligned} \tag{28}$$

In some application scenarios, only the voltage ripple in just one side (LVB or HVB) is needed to be optimized, e.g., the battery energy storage system. In these scenarios, the value of C_2 (or C_1) in (14)–(16) and (18)–(20) can be set to be a very large number so that only the voltage ripple in LVB (or HVB) is actually optimized. The AOCT still can be calculated by (19) and (20). By this means, the optimization of the voltage ripples in both sides transforms into the optimization of the voltage ripple in just one side (LVB or HVB). The tradeoff between the voltage ripple and current stress still can be made in the new AOCT.

D. Comparison of WOCT, COCT, and Conventional Method

1) Control structure: Conventional method is the single-voltage closed-loop control. The double-line-frequency power cannot be controlled arbitrarily. Both WOCT and COCT are feedforward control and open-loop control for double-line-frequency power, as shown in (26) and (27). It is worth noting that only the double-line-frequency power is controlled by WOCT and COCT. Therefore, the control

of average active power in the system is the same as the conventional methods.

2) Optimal objective: Conventional method is aiming at single objective, i.e., minimize the voltage ripple in one side or minimize the low-frequency fluctuations of current. Both WOCT and COCT are based on the optimal trajectory AOCT so that the weighted optimization can be achieved.
3) Optimization effects: Conventional method can only achieve a specific optimization objective. However, $i_{L,\mathrm{peak}}$ is always minimized under any certain $V_{f,\max}$ in AOCT. Therefore, WOCT and COCT not only achieve smooth regulation of $V_{f,\max}$ and $i_{L,\mathrm{peak}}$ but also make the collaborative optimization of $V_{f,\max}$ and $i_{L,\mathrm{peak}}$ possible.
4) Computational burden: Compared with WOCT, COCT does not need to calculate the current stress $i_{L,\mathrm{peak}}$. Moreover, the weighted optimization process is also removed in COCT. Therefore, COCT has much lower computational burden than that in WOCT.
5) Control parameters design: In COCT, the maximum voltage ripple $V_{f,\mathrm{lim}}$ can be limited accurately just by simple calculation. However, in many application scenarios, the values of $V_{f,\mathrm{lim}}$ may not be easy to be determined. $V_{f,\mathrm{lim}}$ is generally set to be the worst allowable value of voltage ripple in the system so that the voltage ripple of COCT always approaches the worst allowable value in most working conditions. Different from COCT, WOCT does not need to set any strict constraint. The weighted factor α only represents the relative magnitude between voltage ripple and current stress. WOCT is more flexible than COCT. However, the weight coefficient α has to be designed empirically.

E. Optimal Control of φ_{10}

In some application scenarios, the initial phase φ_{10} of the single-phase ac load is determined by the load itself. Under this circumstance, φ_{10} cannot be controlled to be accurately synchronized with the grid. In many other application scenarios, φ_{10} can be controlled to synchronize with the grid. However, in most practical applications, φ_{10} is just set to be zero, which means in-phase with the grid voltage for simplicity. As a result, the optimization effects of WOCT and COCT cannot always reach the maximum extent under different load conditions.

The effects of φ_{10} on AOCT are shown in Fig. 13 under the working condition: $U_{s1} = 60$ V, $I_{s1} = 8.33$ A, $P_{\mathrm{load,dc}} = 100$ W, $\varphi_2 = 0^\circ$, $\varphi_1 = 60^\circ$, and variable φ_{10}. As shown in Fig. 13(a), φ_{10} has significant effects on both $V_{f,\max}$ and $i_{L,\mathrm{peak}}$.

The effects of φ_{10} on AOCT are analyzed as follows.

1) The working point GVRM is very sensitive to the variation of φ_{10}, which can be seen from (14) to (16). The maximum range of $V_{f,\max}$ (when $\varphi_{10} = -\pi/6$) is about five times as wide as the minimum range of $V_{f,\max}$ (when $\varphi_{10} = \pi/3$). It indicates that the minimum voltage ripple is susceptible to φ_{10}.
2) The working point AGCSM is not sensitive to the variation of φ_{10}. First, $V_{f,\max}|_{\mathrm{AGCSM}}$ is unrelated to φ_{10}, as shown in (18). Second, $P_{\mathrm{DAB},f}$ is zero at the point AGCSM and only the θ_1 in (11) has a small influence on $i_{L,\mathrm{peak}}$ at AGCSM. It indicates that the minimum $i_{L,\mathrm{peak}}$ is almost not influenced by φ_{10}.

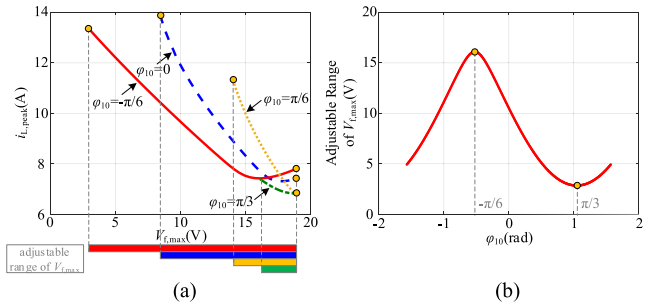

Fig. 13. Effects of φ_{10} on AOCT. (a) AOCT. (b) Adjustable range of $V_{f,\max}$.

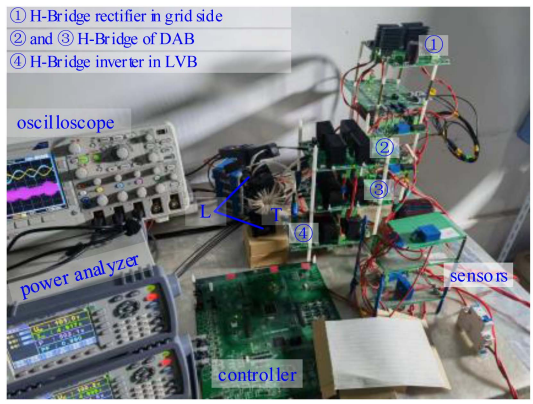

Fig. 14. Schematic diagram of the experimental prototype.

As analyzed above, the most significant effect of φ_{10} on AOCT is the adjustable range of $V_{f,\max}$. If the adjustable range is small, the adaptability and flexibly of WOCT and COCT to different load conditions will be poor. Under the circumstance, the proposed methods are almost the same as the GCSM method [29] and the advantages of the proposed methods cannot be fully exerted.

Therefore, the adjustable range of $V_{f,\max}$ is supposed to be wide as much as possible. According to (16), when $\cos(\varphi_2 - \varphi_1 - 2\varphi_{10}) = 1$, $V_{f,\max}|_{\mathrm{GVRM}}$ reaches its minimum value. The optimal value of φ_{10} can be derived as follows:

$$\varphi_{10} = \frac{\varphi_2 - \varphi_1}{2}. \tag{29}$$

When φ_{10} is controlled by (29), the flexibility and controllability of WOCT and COCT can be maximized.

V. Experimental Results

Based on the topology in Fig. 1, a small-scale prototype (see Fig. 14) was fabricated to verify the proposed OCT and control methods. The single-phase ac load and the pure dc load are added to LVB by an H-bridge inverter and a dc electronic load,

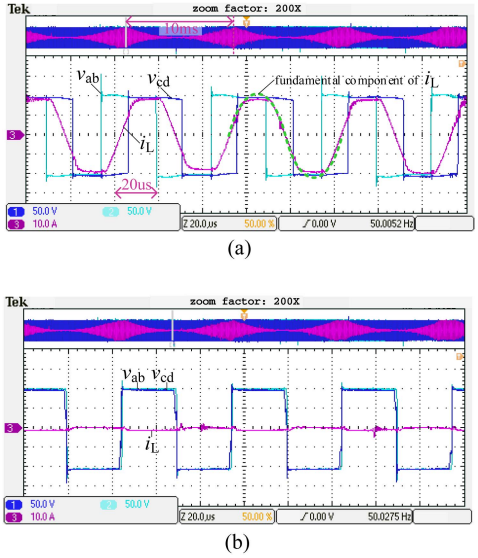

Fig. 15. Details magnification waveforms of v_{ab}, v_{cd}, and i_L in DAB under double-line-frequency fluctuation. (a) Maximum $i_{L,\mathrm{peak}}$. (b) Minimum $i_{L,\mathrm{peak}}$.

respectively. The main parameters of the prototype are shown in Table I.

A. Experimental Verification for OCT

The propagation of low-frequency fluctuations in DAB has been analyzed in [29]. As shown in Fig. 15, in steady-state operation, i_L fluctuates at twice the grid frequency (100 Hz) due to the double-line-frequency fluctuation in the phase-shift ratio of DAB and the dc bus voltage in both sides. The current stress $i_{L,\mathrm{peak}}$ of DAB varies drastically from about 1 to 18 A during a double-line-frequency period. The low-frequency fluctuation of i_L not only increases the current stress of DAB but also deteriorates working efficiency of DAB. The approximate deviation of $i_{L,\mathrm{peak}}$ is inherently produced by the FCA method [30].

As shown in Fig. 16, under the unity power factor single-phase ac load condition, three different control combinations of $P_{\mathrm{DAB}f}$ and γ are applied to control the double-line-frequency power of DAB. The control combination I: $P_{\mathrm{DAB},f} = 200$ W and $\gamma = -0.75$ rad. The control combination II: $P_{\mathrm{DAB},f} = 350$ W and $\gamma = -0.75$ rad. The control combination III: $P_{\mathrm{DAB},f} = 460$ W and $\gamma = -0.82$ rad. The theoretical results and experimental results of voltage ripples and current stress are listed in Table II. Under the three control combinations, the maximum voltage ripple $V_{f,\max}$ almost remains the same, but the current stress $i_{L,\mathrm{peak}}$ differs much, which verifies the theoretical analysis in Fig. 3(a) and (b). The control combination that brings about the minimum $i_{L,\mathrm{peak}}$ is the best one. The OCT is to gather all these optimal working points under different $V_{f,\max}$. The proposed (A)OCT achieves coordination optimization of voltage ripple and current stress over the conventional methods.

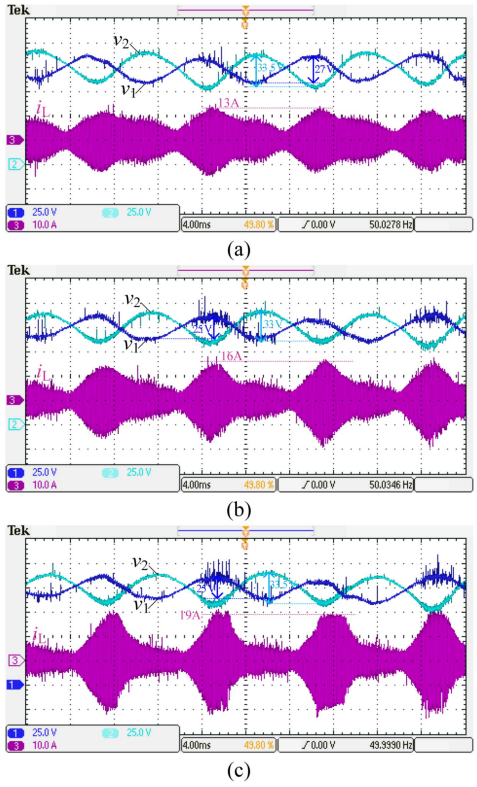

Fig. 16. Voltage ripple and current stress under different control combinations and the same $V_{f,\max}$. Control combinations (a) I. (b) II. (c) III.

TABLE II
VOLTAGE RIPPLE AND CURRENT STRESS UNDER DIFFERENT CONTROL COMBINATIONS

	Control Combinations	$V_{1,\mathrm{f}}$	$V_{2,\mathrm{f}}$	$V_{\mathrm{f,max}}$	$i_{\mathrm{L,peak}}$
Theoretical Results	I	14.8 V	16.1 V	16.1 V	13.1 A
	II	13.9 V	16.2 V	16.2 V	16.5 A
	III	13.4 V	16.3 V	16.3 V	20.4 A
Experimental Results	I	13.5 V	16.75 V	16.75 V	13 A
	II	12.5 V	16.5 V	16.5 V	16 A
	III	12.5 V	16.75 V	16.75 V	19 A

The experimental waveforms of working points in AOCT under unity power factor load condition are shown in Fig. 17. The parameters are $U_{s1} = 60$ V, $I_{s1} = 8.33$ A, $\varphi_1 = 0^\circ$, $P_{\mathrm{load,dc}} = 0$ W, and $\varphi_{10} = \varphi_2 = 0^\circ$. As can be seen in Fig. 17(a)–(f), $i_{L,\mathrm{peak}}$ decreases with the increase of $V_{f,\max}$. The voltage ripple in Fig. 17(f) is about eight times as large as that in Fig. 17(a). The current stress in Fig. 17(a) is about twice as large as that in Fig. 17(f). It indicates that the adjustable ranges of $V_{f,\max}$ and $i_{L,\mathrm{peak}}$ are very wide under unity power factor load condition. Theoretically, the voltage ripples are equal in both sides under unity power factor load condition in AOCT. However, V_{1f} is slightly smaller than V_{2f} by the experimental results in Fig. 17. It is mainly because that the power in HVB side is larger than the power in LVB side due to the power losses in DAB. In most of the range in AOCT, the experimental values of $i_{L,\mathrm{peak}}$ are slightly smaller than the theoretical values. It is mainly because of the approximate deviation of FCA method. As shown in Fig. 17(g), the experimental results of AOCT are highly consistent with the

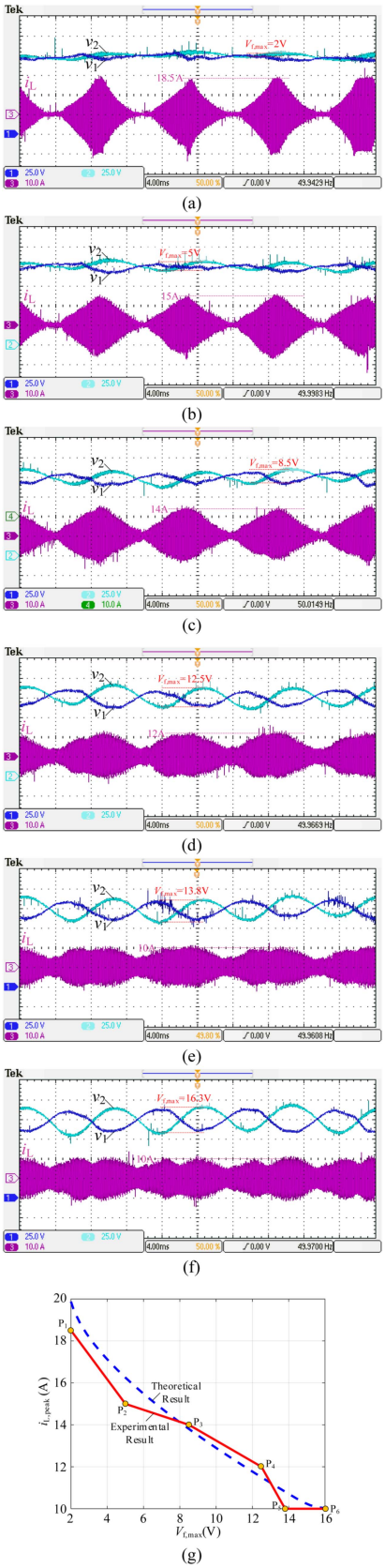

Fig. 17. Experimental results of OCT (AOCT) under unity power factor single-phase AC load condition. (a)–(f) Six working points in AOCT. (g) Comparison of AOCT between the experimental and theoretical results.

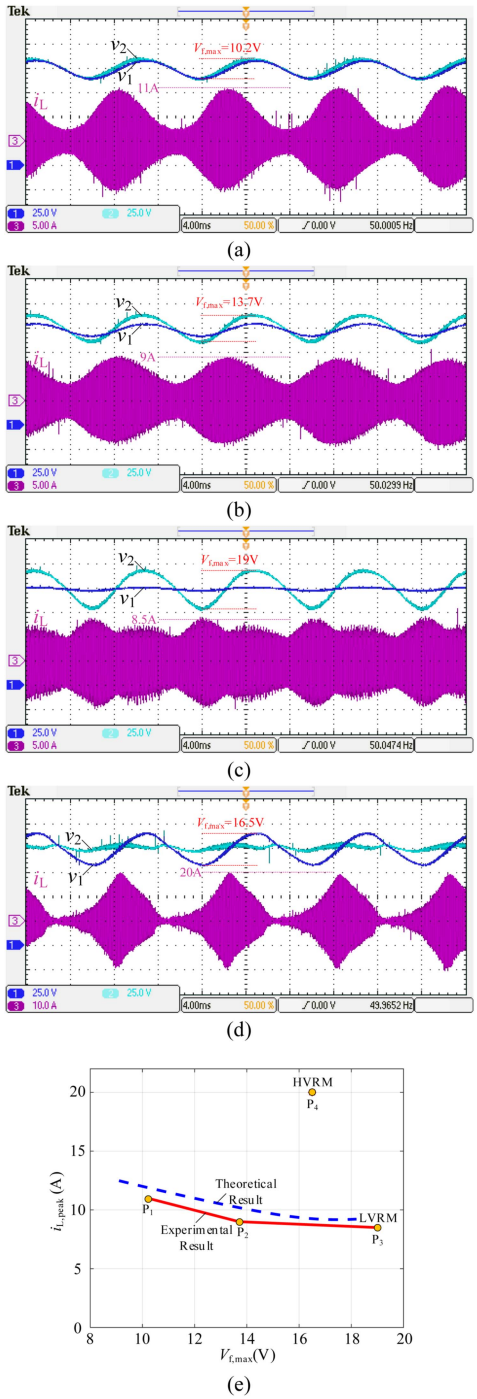

Fig. 18. Experimental results of OCT (AOCT) under pure DC power load condition. (a)–(c) Three working points in AOCT. (d) HVRM. (e) Comparison of AOCT between the experimental and theoretical results.

theoretical results of AOCT. The maximum relative deviation is smaller than 8% and the optimization effects of $V_{f,\max}$ and $i_{L,\text{peak}}$ can be guaranteed. The experimental results verify the correctness and validity of the proposed AOCT under unity power factor load condition.

The experimental waveforms of working points in AOCT under pure dc power load condition are shown in Fig. 18.

TABLE III
VOLTAGE RIPPLE AND CURRENT STRESS UNDER DIFFERENT CONTROL OBJECTIVES

		Conventional Control		Proposed AOCT Control					
		HVRM	LVRM	P_1	P_2	P_3	P_4	P_5	P_6
Unity Power Factor (see Fig. 17)	$V_{f,\max}$	2 V	2 V	2 V	5 V	8.5 V	12.5 V	13.8 V	16.3 V
	$i_{L,\text{peak}}$	18.5 A	18.5 A	18.5 A *GVRM*	15 A	14 A	12 A	10 A	10 A *GCSM*
Pure DC Power (see Fig. 18)	$V_{f,\max}$	16.5 V	19 V	10.2 V	13.7 V	19 V	16.5 V	/	/
	$i_{L,\text{peak}}$	20 A	8.5 A	11 A *GVRM*	9 A	8.5 A *GCSM*	20 A		
Pure Reactive Power (see Fig. 19)	$V_{f,\max}$	17.5 V	17.5 V	9.5 V	12.5 V	15 V	17.5 V	17.5 V	/
	$i_{L,\text{peak}}$	4.5 A	7 A	4 A *GVRM*	4.5 A	4.5 A *GCSM*	4.5 A	7 A	

The parameters are $U_{s1} = 0$ V, $I_{s1} = 0$ A, $\varphi_1 = 0^\circ$, $P_{\text{load,dc}} = 500$ W, and $\varphi_{10} = \varphi_2 = 0^\circ$. The pure dc power load is constructed by a dc electronic load. As shown in Fig. 18(e), the experimental results of AOCT are highly consistent with the theoretical results of AOCT. The experimental results of $i_{L,\text{peak}}$ are slightly lower than the theoretical results, mainly due to the approximate deviation of FCA method. The experimental results verify the correctness and validity of the proposed AOCT under pure dc power load condition.

The experimental waveforms of working points in AOCT under pure reactive power load condition are shown in Fig. 19. The parameters are $U_{s1} = 60$ V, $I_{s1} = 8.33$ A, $\varphi_1 = -90^\circ$, $P_{\text{load,dc}} = 0$ W, and $\varphi_{10} = \varphi_2 = 0^\circ$. The pure inductive power load is constructed by an H-bridge inverter connected with several inductances. In pure reactive power load condition, the active power is supposed to be 0 theoretically. However, there are power losses in the practical devices so that the experimental results of $i_{L,\text{peak}}$ are higher than the theoretical results, as shown in Fig. 19(f). In spite of this, the absolute deviations between the experimental results and the theoretical results of $i_{L,\text{peak}}$ are still small. The small deviations will not deteriorate the steady-state performance of DAB a lot. Moreover, as shown in Fig. 19(a)–(e), the optimization effects of voltage ripples still can be guaranteed. In fact, the power factor of most ac load is relatively high and the pure reactive power load is not common so that the proposed AOCT can be used in most application scenarios. The experimental results verify the correctness and validity of the proposed AOCT under pure reactive power load condition.

The experimental results under different objectives are summarized in Table III. Both HVRM and LVRM are sole working points, which can only adapt to specific load conditions. For example, in Case 3, the HVRM control strategy has the maximum values of $V_{f,\max}$ and $i_{L,\text{peak}}$; in Case 2, the LVRM control strategy has the maximum values of $V_{f,\max}$ and $i_{L,\text{peak}}$. By contrast, AOCT can always achieve minimum voltage ripple or minimum current stress under any load condition. This is because that AOCT consists of a series of optimal working points. Different working points can be used to adapt different demands. Moreover, as can be seen in Table III, there always exists more than one point in AOCT to be superior to HVRM and LVRM in both $V_{f,\max}$ and $i_{L,\text{peak}}$.

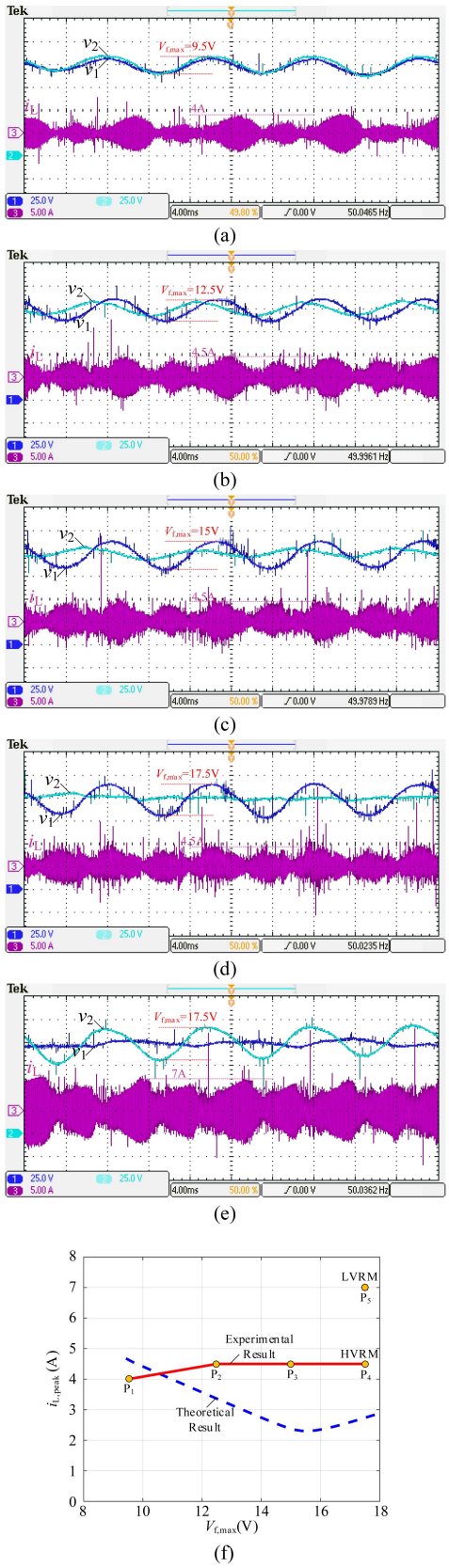

Fig. 19. Experimental results of OCT (AOCT) under pure reactive power single-phase AC load condition. (a)–(d) Four working points in AOCT. (e) LVRM. (f) Comparison of AOCT between the experimental and theoretical results.

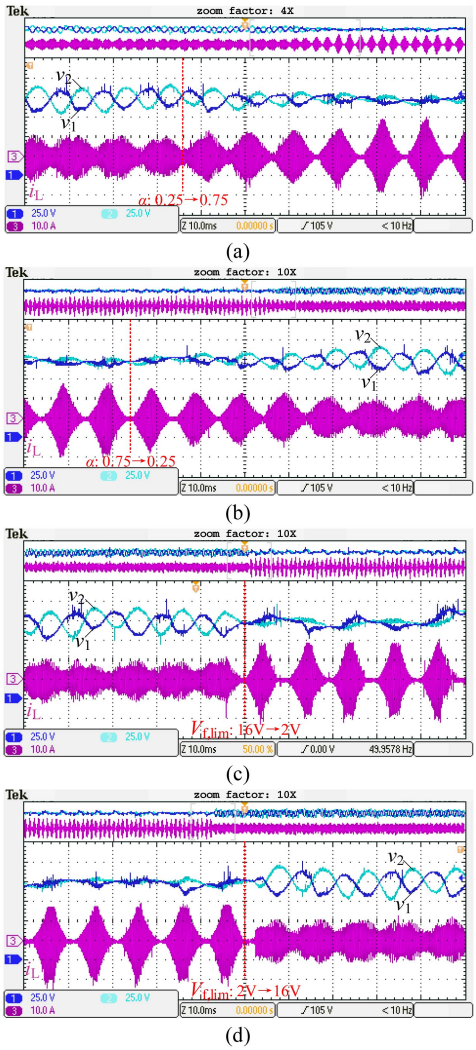

Fig. 20. Experimental results of tradeoff control methods. (a) WOCT α varies from 0.25 to 0.75. (b) WOCT α varies from 0.75 to 0.25. (c) COCT $V_{f,\lim}$ varies from 16 to 2 V. (d) COCT $V_{f,\lim}$ varies from 2 to 16 V.

B. Experimental Verification for Optimal Control Methods

The experimental results of WOCT and COCT control methods under the unity power factor are shown in Fig. 20. The step changes of α and $V_{f,\lim}$ are applied to WOCT and COCT, respectively. As shown in Fig. 20(a) and (b), it takes several double-line-frequency periods for the voltage ripples and current stress to change from the initial steady state to the new steady state by WOCT. As shown in Fig. 20(c) and (d), it takes only one double-line-frequency period for the voltage ripples and current stress to change from the initial steady state to the new steady state by COCT. It demonstrates that the response speed of COCT is much faster than that of WOCT. This is because the complicated calculations of both the real-time current stress in (23) and the hill-climbing searching method are not needed in COCT. By these two methods, the voltage ripples and current stress can be adjusted flexibly according to the actual working conditions. The experimental results verify the correctness and validity of the proposed tradeoff control methods.

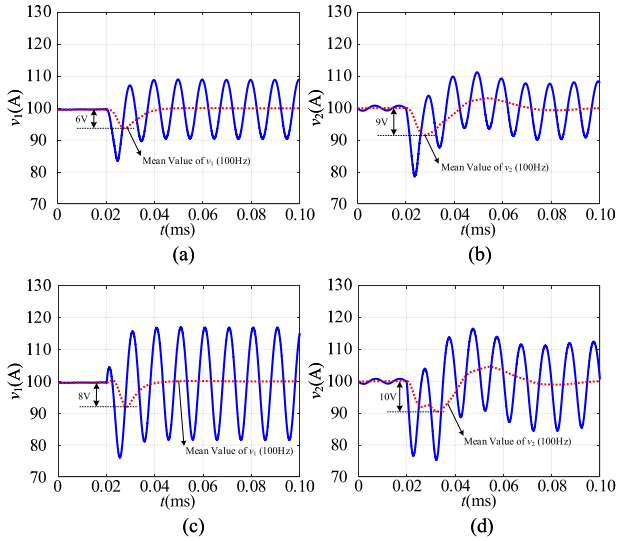

Fig. 21. Simulation results of the impact of the proposed control system on converter's dynamics in case 4. (a) and (b) Step change of load at GVRM point ($P_{\mathrm{DAB}f,\mathrm{opt}} = 340$ W and $\gamma_{\mathrm{opt}} = -0.98$ rad). (c) and (d) Step change of load at GCSM point ($P_{\mathrm{DAB}f,\mathrm{opt}} = 50$ W and $\gamma_{\mathrm{opt}} = -0.79$ rad).

In order to discover the impact of the proposed control system on the converter's dynamics, some simulation results are shown in Fig. 21. The closed-loop control parameters in the control system of dc/ac and dc/dc are fixed; only the parameters of the "feedforward compensation," i.e., $P_{\mathrm{DAB}f,\mathrm{opt}}$ and γ_{opt}, can be adjusted so that the impact of the proposed control system on the converter's dynamics can be observed. The GVRM and GCSM working points in Case 4 are selected for simulation. When $t < 0.02$ s, no load in the LVdc side. After $t = 0.02$ s, the ac load and the dc load in Case 4 are added to the LVdc side (step change) and the feedforward compensation is implemented. As shown in Fig. 21, the proposed control method will not change the dynamic performance of the system significantly. It is mainly because the proposed control is "feedforward control" and the feedforward control will not change the poles of the closed-loop system. The control parameters design method of the proposed control method is the same as that of the conventional single-voltage closed-loop control method.

C. Experimental Results of Working Efficiency in AOCT

The variation ranges of $V_{f,\max}$ and $i_{L,\mathrm{peak}}$ reach their maximum extents under unity power factor load condition. Therefore, the most obvious variation of working efficiency also occurs under unity power factor load condition. As shown in Fig. 22, the working efficiency increases with the increase of voltage ripple and the decrease of current stress. It indicates that the optimization of voltage ripples and the optimization of current stress are two contradictory objectives. The highest efficiency, which occurs near to the point AGCSM, is 96.5%. The lowest efficiency, which occurs near to the point GVRM, is 92.3%. The 4% variation of working efficiency has significant influence on the steady-state performance of DAB. The experimental results demonstrate the practical significance of tradeoff control

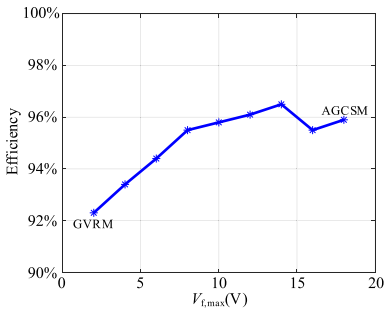

Fig. 22. Experimental results of DAB working efficiency in AOCT under unity power factor single-phase ac load condition.

between voltage ripple and current stress in two-stage single-phase system. As can be seen in Fig. 22, the efficiency slightly decreases when the working point is very close to the AGCSM. It is because the large voltage ripples may increase the switching losses in the system. The $V_{f,\max}$ of the highest efficiency point is about 75% of the $V_{f,\max}$ of AGCSM.

VI. Conclusion

In this article, the optimization of DAB current stress and the flexible tradeoff between the current stress and the voltage ripples in a single-phase two-stage converter system are achieved by controlling the double-line-frequency power in DAB. The theoretical analysis and experimental results indicate the following conclusions.

1) The conventional control methods generally can only achieve the optimization of either the dc bus voltage ripple or the dc/dc current stress. Moreover, the optimal results of the conventional control methods generally are fixed working points so that the current stress and voltage ripples cannot be adjusted flexibly. By contrast, the proposed methods achieve both the optimization and the flexible tradeoff of current stress and voltage ripples.
2) There are various control combinations of double-line-frequency power in DAB corresponding to a certain value of voltage ripple. These optimal working points in OCT always can achieve minimum current stress under certain voltage ripple. Theoretical analysis indicates that AOCT is a good approximation of OCT with simple calculations. The experimental results verify good optimization effects of AOCT.
3) The feasibility and effectiveness of the proposed WOCT and COCT methods are verified by the experimental results. Both the current stress and the voltage ripples can be adjusted flexibly by these two methods. The working efficiency of OCT has been measured by experimental methods. The working efficiency increases with the increase of voltage ripple and the decrease of current stress. The difference between the highest efficiency and the lowest efficiency is about 4%. It indicates that the tradeoff control between current stress and voltage ripple is worth making to adapt various load conditions and working conditions.

References

[1] M. Kasper, D. Bortis, G. Deboy, and J. W. Kolar, "Design of a highly efficient (97.7%) and very compact (2.2 kW/dm^3) isolated AC–DC telecom power supply module based on the multicell ISOP converter approach," *IEEE Trans. Power Electron.*, vol. 32, no. 10, pp. 7750–7769, Oct. 2017, doi: 10.1109/TPEL.2016.2633334.

[2] J. Yuan, L. Dorn-Gomba, A. D. Callegaro, J. Reimers, and A. Emadi, "A review of bidirectional on-board chargers for electric vehicles," *IEEE Access*, vol. 9, pp. 51501–51518, 2021, doi: 10.1109/ACCESS.3069448.

[3] D. D. Atkar, P. Chaturvedi, H. M. Suryawanshi, P. P. Nachankar, and D. Yadeo, "Optimal design of solid state transformer-based interlink converter for hybrid AC/DC micro-grid applications," *IEEE J. Emerg. Sel. Topics Power Electron.*, vol. 10, no. 4, pp. 3685–3696, Aug. 2022, doi: 10.1109/JESTPE.2021.3099625.

[4] B. Zhao, X. Zhang, and J. Huang, "AI algorithm-based two-stage optimal design methodology of high-efficiency CLLC resonant converters for the hybrid AC–DC microgrid applications," *IEEE Trans. Ind. Electron.*, vol. 66, no. 12, pp. 9756–9767, Dec. 2019, doi: 10.1109/TIE.2019.2896235.

[5] H. Shi, K. Sun, Y. W. Li, and H. Wu, "A closed-loop DC-transformer control method for dual-active-bridge interlinking converters in DC microgrids," *CSEE J. Power Energy Syst.*, to be published, doi: 10.17775/CSEEJPES.2021.08010.

[6] H. Qin and J. W. Kimball, "Closed-loop control of DC-DC dual active bridge converters driving single-phase inverters," in *Proc. IEEE Energy Convers. Congr. Expo.*, 2012, pp. 173–179.

[7] B. Zhao, Q. Song, and W. Liu, "A practical solution of high-frequency-link bidirectional solid-state transformer based on advanced components in hybrid microgrid," *IEEE Trans. Ind. Electron.*, vol. 62, no. 7, pp. 4587–4597, Jul. 2015, doi: 10.1109/TIE.2014.2350459.

[8] Z. Li et al., "A second-harmonic suppression method based on differentiated-capacitance design for input-parallel output-series DAB fed single-phase VSI," *IEEE Trans. Power Electron.*, vol. 37, no. 10, pp. 11592–11606, Oct. 2022, doi: 10.1109/TPEL.2022.3167735.

[9] A. R. Gautam, D. M. Fulwani, R. R. Makineni, A. K. Rathore, and D. Singh, "Control strategies and power decoupling topologies to mitigate 2ω-ripple in single-phase inverters: A review and open challenges," *IEEE Access*, vol. 8, pp. 147533–147559, 2020, doi: 10.1109/ACCESS.2020.3015315.

[10] B. Guo et al., "Optimization design and control of single-stage single-phase PV inverters for MPPT improvement," *IEEE Trans. Power Electron.*, vol. 35, no. 12, pp. 13000–13016, Dec. 2020, doi: 10.1109/TPEL.2020.2990923.

[11] Y. Liu, W. Zhang, Y. Sun, M. Su, G. Xu, and H. Dan, "Review and comparison of control strategies in active power decoupling," *IEEE Trans. Power Electron.*, vol. 36, no. 12, pp. 14436–14455, Dec. 2021, doi: 10.1109/TPEL.2021.3087170.

[12] T. Isobe, R. A. Barrera-Cardenas, Z. He, Y. Zou, K. Terazono, and H. Tadano, "Control of three-phase solid-state transformer with phase-separated configuration for minimized energy storage capacitors," *IEEE J. Emerg. Sel. Topics Power Electron.*, vol. 8, no. 3, pp. 3014–3028, Sep. 2020, doi: 10.1109/JESTPE.2019.2923785.

[13] X. Liu and H. Li, "An electrolytic-capacitor-free single-phase high-power fuel cell converter with direct double-frequency ripple current control," *IEEE Trans. Ind. Appl.*, vol. 51, no. 1, pp. 297–308, Jan./Feb. 2015, doi: 10.1109/TIA.2014.2326085.

[14] L. Xue, Z. Shen, D. Boroyevich, P. Mattavelli, and D. Diaz, "Dual active bridge-based battery charger for plug-in hybrid electric vehicle with charging current containing low frequency ripple," *IEEE Trans. Power Electron.*, vol. 30, no. 12, pp. 7299–7307, Dec. 2015, doi: 10.1109/TPEL.2015.2413815.

[15] T. Zhao, X. She, S. Bhattacharya, G. Wang, F. Wang, and A. Huang, "Power synchronization control for capacitor minimization in solid state transformers (SST)," in *Proc. IEEE Energy Convers. Congr. Expo.*, 2011, pp. 2812–2818.

[16] M. Ali, M. Yaqoob, L. Cao, and K. H. Loo, "Disturbance-observer-based DC-bus voltage control for ripple mitigation and improved dynamic response in two-stage single-phase inverter system," *IEEE Trans. Ind. Electron.*, vol. 66, no. 9, pp. 6836–6845, Sep. 2019, doi: 10.1109/TIE.2018.2879294.

[17] Y.-T. Huang, C.-C. Yang, T.-S. Li, and Y.-M. Chen, "A feedforward voltage control strategy for reducing the output voltage double-line-frequency ripple in single-phase AC–DC converters," *IEEE J. Emerg. Sel. Topics Power Electron.*, vol. 9, no. 6, pp. 6605–6612, Dec. 2021, doi: 10.1109/JESTPE.2021.3083258.

[18] L. Meng et al., "Optimal input and output power quality control of single-phase AC–DC–DC converter with significant DC-link voltage ripple," *IEEE Trans. Ind. Electron.*, vol. 67, no. 12, pp. 10366–10376, Dec. 2020, doi: 10.1109/TIE.2019.2958310.

[19] M. Fawzi, I. Abdelsalam, A. A. Aboushady, and S. A. A. Maksoud, "A modified phase shift control of the dual active bridge-based modular power electronic transformer to minimize the LVdc side voltage ripples under unbalanced load conditions," *IEEE Access*, vol. 10, pp. 81309–81322, 2022, doi: 10.1109/ACCESS.2022.3195941.

[20] J. Teng, Z. Bu, X. Sun, H. Fu, W. Zhao, and X. Li, "Common high-frequency bus-based cascaded multilevel solid-state transformer with ripple and unbalance power decoupling channel," *IEEE Trans. Power Electron.*, vol. 37, no. 8, pp. 9345–9361, Aug. 2022, doi: 10.1109/TPEL.2022.3153367.

[21] J. Zhou et al., "Design and control of power fluctuation delivery for cell capacitance optimization in multiport modular solid-state transformers," *IEEE Trans. Power Electron.*, vol. 36, no. 2, pp. 1412–1427, Feb. 2021, doi: 10.1109/TPEL.2020.3006956.

[22] Z. Yang, J. Sun, X. Zha, and Y. Tang, "Power decoupling control for capacitance reduction in cascaded-H-bridge-converter-based regenerative motor drive systems," *IEEE Trans. Power Electron.*, vol. 34, no. 1, pp. 538–549, Jan. 2019, doi: 10.1109/TPEL.2018.2818719.

[23] F. Xiao, C. Tu, Q. Ge, K. Zhou, Q. Guo, and Z. Lan, "Ripple voltage suppression and control strategy for CHB-based solid-state transformer," *IEEE J. Emerg. Sel. Topics Power Electron.*, vol. 9, no. 1, pp. 1104–1118, Feb. 2021, doi: 10.1109/JESTPE.2019.2959786.

[24] L. Zhang and X. Ruan, "Control schemes for reducing second harmonic current in two-stage single-phase converter: An overview from DC-bus port-impedance characteristics," *IEEE Trans. Power Electron.*, vol. 34, no. 10, pp. 10341–10358, Oct. 2019, doi: 10.1109/TPEL.2019.2894647.

[25] A. R. Gautam, K. Gourav, J. M. Guerrero, and D. M. Fulwani, "Ripple mitigation with improved line-load transients response in a two-stage DC–DC–AC converter: Adaptive SMC approach," *IEEE Trans. Ind. Electron.*, vol. 65, no. 4, pp. 3125–3135, Apr. 2018, doi: 10.1109/TIE.2017.2752125.

[26] H. Zhou, L. He, and Z. Lin, "Low frequency current ripple suppression for two-stage single-phase inverter based on impedance editing," *IEEE Trans. Ind. Electron.*, vol. 69, no. 12, pp. 13417–13427, Dec. 2022, doi: 10.1109/TIE.2021.3128913.

[27] T. Zhao et al., "Analysis and suppression of resonant current envelope ripple of LLC converter in cascaded modular PV solid-state transformer," *IEEE J. Emerg. Sel. Topics Power Electron.*, vol. 9, no. 3, pp. 3744–3757, Jun. 2021, doi: 10.1109/JESTPE.2020.2988989.

[28] Y. Hu et al., "High-frequency-link current stress optimization of cascaded H-bridge-based solid-state transformer with third-order harmonic voltage injection," *IEEE J. Emerg. Sel. Topics Power Electron.*, vol. 9, no. 1, pp. 1027–1038, Feb. 2021, doi: 10.1109/JESTPE.2020.2965232.

[29] F. Xiong, J. Li, D. Yan, and X. Chen, "Current stress optimization of dual active bridge converter in two-stage single-phase inverter system with second harmonic current shaping," *IEEE Trans. Power Electron.*, vol. 37, no. 3, pp. 2606–2624, Mar. 2022, doi: 10.1109/TPEL.2021.3110110.

[30] B. Zhao, Q. Song, W. Liu, G. Liu, and Y. Zhao, "Universal high-frequency-link characterization and practical fundamental-optimal strategy for dual-active-bridge DC-DC converter under PWM plus phase-shift control," *IEEE Trans. Power Electron.*, vol. 30, no. 12, pp. 6488–6494, Dec. 2015, doi: 10.1109/TPEL.2015.2430934.

[31] J. Peng, B. Fan, and W. Liu, "Penalty-based distributed optimal control of DC microgrids with enhanced current regulation performance," *IEEE Trans. Circuits Syst. I, Reg. Papers*, vol. 69, no. 7, pp. 3026–3036, Jul. 2022, doi: 10.1109/TCSI.2022.3167790.

[32] X. Xiao, X. Huang, and Q. Kang, "A hill-climbing-method-based maximum-power-point-tracking strategy for direct-drive wave energy converters," *IEEE Trans. Ind. Electron.*, vol. 63, no. 1, pp. 257–267, Jan. 2016, doi: 10.1109/TIE.2015.2465964.

Fei Xiong (Member, IEEE) received the B.S. and Ph.D. degrees in electrical engineering from Beijing Jiaotong University, Beijing, China, in 2013 and 2018, respectively.

He is currently with the Chongqing University of Posts and Telecommunications, Chongqing, China. His research interests include power electronics technology, energy storage, ac/dc microgrid, and power converter.

Peng Wu was born in Sichuan, China, in 1998. He received the B.S. degree from the School of Electrical and Information Engineering, Henan University of Engineering, Zhengzhou, China, in 2020, and the M.S. degree from the School of Automation, Chongqing University of Posts and Telecommunications, Chongqing, China, in 2023.

His research interests include two-stage ac/dc power electronic transformers.

Hongyu Yang was born in Chongqing, China, in 1998. He received the B.S. degree in engineering and the M.S. degree in electronic information from the College of Automation, Chongqing University of Posts and Telecommunications, Chongqing, China, in 2020 and 2023, respectively.

He is currently engaged in high-power ac–dc converter research and design. His main research interest focuses on power electronic transformer technology.

Kaibi Zhang received the B.S. degree in computer engineering from the Shandong University of Science and Technology, Qingdao, China, in 1996, and the M.S. degree in computer technology from the Chongqing University of Posts and Telecommunications, Chongqing, China, in 2008.

She is currently an Associate Professor with the School of Automation, Chongqing University of Posts and Telecommunications. Her research interests include Automatic control, computer, and application.

Dong Yan received the B.S. degree from the Harbin University of Science and Technology, Harbin, China, in 2001, and the master's and Ph.D. degrees from the Harbin Institute of Technology, Harbin, in 2003 and 2007, respectively, all in electric engineering.

He is currently a Professor with the Chongqing University of Posts and Telecommunications, Chongqing, China. His research interests include energy routers and self-powered sources.